PhD Thesis

Investigation of complex liquid-gas turbulent interfacial flows

A Numerical Study

Sagar Pal

June 26, 2020

Institut Jean le Rond ∂'Alembert
Sorbonne Université

PhD Thesis

Disclaimer
You can edit this page to suit your needs. For instance, here we have a no copyright statement, a colophon and some other information. This page is based on the corresponding page of Ken Arroyo Ohori's thesis, with minimal changes.

Colophon
This document was typeset with the help of KOMA-Script and LaTeX using the kaobook class.
The source code of this book is available at:
https://github.com/fmarotta/kaobook
(You are welcome to contribute!)

Publisher
First printed in May 2019 by Institut Jean le Rond ∂'Alembert
Sorbonne Université

The harmony of the world is made manifest in Form and Number, and the heart and soul and all the poetry of Natural Philosophy are embodied in the concept of mathematical beauty.

– D’Arcy Wentworth Thompson

Contents

List of Figures

List of Tables

Introduction | 1

Multiphase Flows

Brief description of multiphase flows in nature Hello, here is some text without a meaning. This text should show what a printed text will look like at this place. If you read this text, you will get no information. Really? Is there no information? Is there a difference between this text and some nonsense like “Huardest gefburn”? Kjift – not at all! A blind text like this gives you information about the selected font, how the letters are written and an impression of the look. This text should contain all letters of the alphabet and it should be written in of the original language. There is no need for special content, but the length of words should match the language.

Surface tension dominated flows Hello, here is some text without a meaning. This text should show what a printed text will look like at this place. If you read this text, you will get no information. Really? Is there no information? Is there a difference between this text and some nonsense like “Huardest gefburn”? Kjift – not at all! A blind text like this gives you information about the selected font, how the letters are written and an impression of the look. This text should contain all letters of the alphabet and it should be written in of the original language. There is no need for special content, but the length of words should match the language.

Fragmentation

Brief description of atomization Hello, here is some text without a meaning. This text should show what a printed text will look like at this place. If you read this text, you will get no information. Really? Is there no information? Is there a difference between this text and some nonsense like “Huardest gefburn”? Kjift – not at all! A blind text like this gives you information about the selected font, how the letters are written and an impression of the look. This text should contain all letters of the alphabet and it should be written in of the original language. There is no need for special content, but the length of words should match the language.

Importance of drop size distributions Hello, here is some text without a meaning. This text should show what a printed text will look like at this place. If you read this text, you will get no information. Really? Is there no information? Is there a difference between this text and some nonsense like “Huardest gefburn”? Kjift – not at all! A blind text like this gives you information about the selected font, how the letters are written and an impression of the look. This text should contain all letters of the alphabet and it should be written in of the original language. There is no need for special content, but the length of words should match the language.

Numerical Platforms

PARIS Simulator Hello, here is some text without a meaning. This text should show what a printed text will look like at this place. If you read this text, you will get no information. Really? Is there no information? Is there a difference between this text and some nonsense like "Huardest gefburn"? Kjift – not at all! A blind text like this gives you information about the selected font, how the letters are written and an impression of the look. This text should contain all letters of the alphabet and it should be written in of the original language. There is no need for special content, but the length of words should match the language.

Basilisk Hello, here is some text without a meaning. This text should show what a printed text will look like at this place. If you read this text, you will get no information. Really? Is there no information? Is there a difference between this text and some nonsense like "Huardest gefburn"? Kjift – not at all! A blind text like this gives you information about the selected font, how the letters are written and an impression of the look. This text should contain all letters of the alphabet and it should be written in of the original language. There is no need for special content, but the length of words should match the language.

Numerical Development

Methodology 2

In this chapter, we describe the basic numerical methodology behind our models concerning the dynamics of immiscible liquid-gas interfacial flows, at the incompressible and isothermal limits. These implementations are developed on the platforms 'PARIS Simulator' [1] and 'Basilisk' [2], with considerable overlap between the two platforms in terms of the treatment of the interface capturing schemes, transport of conserved quantities and surface tension models. [1] The numerical implementations are based on finite volume discretizations on uniform or dynamically refined Cartesian grids , utilizing state of the art methods in interfacial reconstruction coupled with geometric transport of the corresponding fluxes, curvature computation and surface tension modeling. For more detailed descriptions of the general capabilities of 'PARIS Simulator' and 'Basilisk', we refer the reader to the previously cited references.

1: The principle difference between 'PARIS Simulator' and 'Basilisk' is the ability to resolve the conservation laws on dynamically adaptive meshes in the case of 'Basilisk', whereas 'PARIS Simulator' only deals with regular Cartesian meshes.

2.1 Governing Equations

We use the one-fluid formulation for our system of governing equations, thus solving the incompressible Navier-Stokes equations throughout the whole domain including regions of variable density and viscosity, which itself depend on the explicit location of the interface separating the two fluids. In the absence of mass tranfer, the velocity field is continuous across the interface at the incompressible limit, with the interface evolving according to the local velocity vector.

Conservative Formulation

Generally, we have a choice regarding how to model the convective operator of the incompressible Navier-Stokes equations. There is a well established corpus of numerical methods tailored specifically to deal with non-conservative [2] form of the convective operator that appear in transport equations of mass and momentum [3] , which perform quite well in the context of single phase flows. However, in interfacial flows we often deal with discontinuities that arise as a consequence of the contrast in material properties between the two fluids. Therefore, even though the velocity field remains continuous throughout the domain, the otherwise smooth density (mass) and momentum fields contain sharp jumps (discontinuities) localized at the interfacial position. Therefore, we choose to formulate our governing equations in a conservative form i.e involving divergence of fluxes instead of gradients of the primitive variables when it comes to the convective operator. More detailed discussions and analyses about the comparative advantages of the conservative formulation in the context of flows involving large density-ratios is the focus of the subsequent chapters. Thus, the equations are as follows :

2: also referred to as the strong form, necessitating certain orders of smoothness of the primitive variable

3: These methods are descendants of the class of numerical schemes used to solve hyperbolic partial differential equations.

$$\frac{\partial \rho}{\partial t} + \nabla \cdot (\rho \boldsymbol{u}) = 0 \tag{2.1}$$

$$\frac{\partial}{\partial t} (\rho \boldsymbol{u}) + \nabla (\rho \boldsymbol{u} \otimes \boldsymbol{u}) = -\nabla p + \nabla \cdot (2\mu \boldsymbol{D}) + \sigma \kappa \delta_s \boldsymbol{n} + \rho \boldsymbol{g} \tag{2.2}$$

with ρ and μ being the density and dynamical viscosity respectively, and therefore are the physical quantities which are discontinuous across the interface. The volumetric sources are modeled by the acceleration g, and the deformation rate tensor $\boldsymbol{D}$ used to model the viscous stresses is defined as:

$$\boldsymbol{D} = \frac{1}{2} \left[\nabla \boldsymbol{u} + (\nabla \boldsymbol{u})^T \right] \tag{2.3}$$

The term $\sigma \kappa \delta_s \boldsymbol{n}$ models the surface tension forces in the framework of the continuum surface-force (CSF) method. The normal vector to the interface is $\boldsymbol{n}$, with σ being the coefficient of surface tension and κ the local interfacial curvature. The operator δ_s is the Dirac delta function, the numerical approximation of which allows us to map the singular surface force distribution along the interface onto their volumetric equivalents for our Cartesian control volumes. At the incompressible limit, the advection of mass given by equation 2.1 can be treated as equivalent to that of the advection of volume.

Material Properties

Within the framework of interface capturing schemes, the temporal evolution of the interface separating the two fluids can be modeled by the following advection equation :

$$\frac{\partial \chi}{\partial t} + \boldsymbol{u} \nabla \chi = 0 \tag{2.4}$$

where χ is the phase-characteristic function, that has different values in each phase [4] . Mathematically, the function χ is equivalent to a Heaviside function in space and time. At the macroscopic length scales under consideration, the interface evolution as described by equation 2.4 is modeled as having infinitesimal thickness under the continuum hypothesis. The coupling of the interfacial evolution with the equations of fluid motion as described in 2.1 and 2.2 is provided by :

4: Generally, χ is assigned values of 0 in one phase and 1 in the other.

$$\rho = \rho_1 \chi + (1 - \chi) \rho_2 \tag{2.5}$$

$$\mu = \mu_1 \chi + (1 - \chi) \mu_2 \tag{2.6}$$

where ρ_1, ρ_2 are the densities of fluids 1 and 2 respectively, likewise for viscosities μ_1 and μ_2. Under certain circumstances, it is beneficial to opt for a weighted harmonic mean description of the variable dynamic viscosity, instead of the weighted arithmetic mean as in equation 2.6.

The two main (and the most popular) approaches in the context of interface capturing schemes are the are the volume-of-fluid (VOF) method first developed by Hirt and Nichols [3], and the level set class of methods pioneered by Osher and Sethian [4]. The principal difference between the two approaches lies in the manner in which the Heaviside function χ is modeled in the discrete sense, either as a smooth differentiable field in the case of level sets, or as a sharp discontinuous field in the volume-of-fluid (VOF) context. Each class of methods has its own set of merits (and demerits) relative to each other. Generally speaking, volume-of-fluid based methods display superior mass conservation [5] whereas in terms of interface curvature computation, level set based methods hold an advantage [6] . A detailed exposition into the different classes of interfacial transport methods can be found in the seminal monograph by Tryggvason, Scardovelli and Zaleski [5]

5: VOF based methods implicitly track the evolution of the discontinuous density field, which is not the case in level set based methods.

6: The differentiable nature of the level set function lends itself to straightforward curvature computation routines.

2.2 Interfacial Transport : VOF

Our numerical studies are based on the Volume-of-Fluid methodology. We refer to the discontinuous approximation to the Heaviside function [7] χ as the volume fraction field or colour function interchageably, which is defined below in the context of finite volume discretization :

7: A comprehensive discussion about the different types of approximations to the interface Heaviside function can be found in Popinet [6]

$$C_{ijk}(t) = \frac{1}{\Delta V} \int_{\Delta V} \chi(\boldsymbol{x}, t)\, d\boldsymbol{x} \tag{2.7}$$

where C is the colour function with its values lying between 0 and 1, with i,j and k being the indices to the corresponding discretized control volume of volume ΔV. There are two steps involved in the VOF method, the reconstruction of the interface and its subsequent propagation (advection). We present a brief overview of the two steps in the following sections, as going into detailed descriptions of the reconstruction and propagation procedures are not the focus of the present body of work [8] .

8: In-depth explanations into these numerical techniques can be found in [5, 7–9].

PLIC representation

We employ means of geometric reconstructions to explicitly define the interface location using the discrete colour function information. The interface is represented by disjointed line segments under the PLIC (piecewise linear interface construction) framework as illustrated in figure 2.1, with the images reproduced from the the review by Scardovelli and Zaleski [7] . Such reconstructions involve the determination of interface normals using the Mixed Youngs Centered method, the detailed description of which can be found in [5].

[7]: Scardovelli et al. (1999), 'Direct nu ical simulation of free-surface and int cial flow'

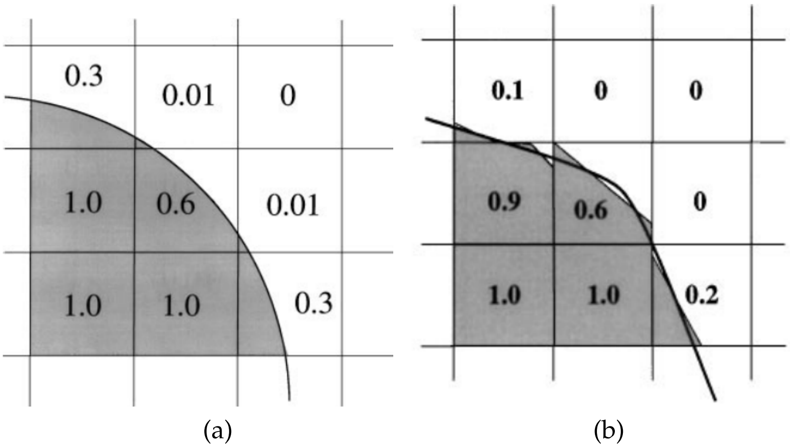

Figure 2.1: Exlicit definition of the interface location using the volume-of-fluid approach. These images are reproduced with permission from Scardovelli and Zaleski [7]. (a) The exact discrete representation of a circular arc on a regular Cartesian grid using the colour function field (volume fraction). (b) The piecewise linear (PLIC) approximation to the smooth circular arc shown in (a), which entails second-order spatial accuracy.

Flux Computation

Once the geometric PLIC reconstructions have been carried out, the interface segments are advected using the the velocity field. This entails computation of fluxes of the colour function, which can be computed via algebraic transport schemes (generally less accurate), or by using geometric reconstructions in either Eulerian, Lagrangian or hybrid frameworks. In the context of our numerical platforms ('PARIS' and 'Basilisk'), state-of-the-art [9] geometrical flux reconstruction procedues are utilised. The temporal integration of the fluxes could be carried out either as a series of one dimensional propagations along each of the spatial directions, termed as direction-split, or carried out in one single sweep, termed as multidimensional or unsplit.

9: The reader can refer to [1, 2] for further details

Direction-split methods are more intuitive and easier to develop (extension to 3D in particular), but suffer from lack of conservation (to the order of machine precision) when it comes to 3D [10] . Multidimensional (unsplit) methods have an advantage in that respect due to the fact that they are conservative by nature of their design, but are inherently more complicated to develop and implement, with no straightforward extension from 2D to 3D. For a more detailed and nuanced evaluation of the comparitive advantages of interfacial transport methods, we refer the reader to the recent review by Mirjalili et al. [11] on the given subject. The propagation of the interface can be described by the evolution of the colour function (volume fraction field) as -

10: A detailed exposition of this problem along with a noteworthy solution can be found in the work by Weymouth and Yue [10]

$$\frac{\partial C}{\partial t} + \boldsymbol{u} \cdot \nabla C = 0 \tag{2.8}$$

We can express the same in the conservative form as -

$$\frac{\partial C}{\partial t} + \nabla \cdot (C\boldsymbol{u}) = C\,(\nabla \cdot \boldsymbol{u}) \tag{2.9}$$

As one can observe, the "compression" term on the right hand side of equation 2.9 equals to zero in the context of incompressible flows without mass transfer, but it is important to keep this term in our numerical formulation within the direction-split framework. Discretization of the above equation results in :

$$C_{i,j,k}^{n,d+1} = C_{i,j,k}^{n,d} - F_{+}^{n,d}(C) - F_{-}^{n,d}(C) + \overline{C}_{i,j,k}^{n,d}\left(\frac{\Delta u_q}{\Delta x}\right)_{i,j,k}^{n,d} \tag{2.10}$$

The above equation represents an advection substep, the superscripts n and d refer to the timestep and direction of integration respectively. The notation $d = 0$ refers to the field at the n^{th} timestep, before any integration is performed along any direction. The fluxes $F_{\pm}^{n,d}(C)$ in equation 2.10 are derived through geometrical reconstructions [11] . The + and − subcripts refer to the orientation with respect to the central cell (i, j, k). The subscript q refers to the direction corresponding to that given advection substep i.e either X, Y or Z. In our case, our numerical platforms are based on cubic (regular Cartesian) grids, consequently there is no requirement for a subscript with Δx. After each substep, the interface is reconstructed once again with the updated volume fraction field in order to compute the fluxes for the next advection substep. Finally, the volume fraction field for the next timestep is given by -

11: For details regarding geometric flux reconstruction, refer to [5, 7]

$$C_{i,j,k}^{n+1} = C_{i,j,k}^{n,3} \tag{2.11}$$

The interpretation and numerical approximation of the prefactor $\overline{C}_{i,j,k}^{n,d}$ to the directional divergence, as well as the fluxes $F_{\pm}^{n,d}(C)$, depend on the exact nature of the geometrical advection scheme in question, which in our context is either CIAM (Lagrangian explicit) or Weymouth-Yue (Eulerian implicit) [12] . A brief outline of these two methods is presented in the subsequent sections.

12: The classification of Lagrangian explicit and Eulerian implicit are in accordance with the paper by Aulisa et al. [12]

Lagrangian Explicit This scheme was originally described in the work of Li [13], 'CIAM' being an abbreviation for the French title '*Calcul d'interface affine par morceaux*', which can be thought of as a straightforward Lagrangian transport of the interface Heaviside function. After the interface segments are reconstructed from the discrete colour function at the start of the time-step, the interfacial points are transported by the component of the velocity field corresponding to the direction of transport. A geometrical interpretation of the scheme is illustrated in figure 2.2, reproduced from the seminal work of Gueyffier et al. [14].

As one can infer from the geometrical representation in figure 2.2, the fluxes $F_{\pm}^{n,d}(C)$ correspond to the volumes Φ^- and Φ^+. Thus, the updated field $C_{i,j,k}^{n,d+1}$ is the sum of the three contributions Φ^- , Φ^0 and Φ^+. We can rewrite equation 2.10 specifically for the CIAM scheme as -

$$C_{i,j,k}^{n,d+1} = C_{i,j,k}^{n,d}\left[1 + \left(\frac{\Delta u_q}{\Delta x}\right)_{i,j,k}^{n,d}\right] - F_{+}^{n,d}(C) - F_{-}^{n,d}(C) \tag{2.12}$$

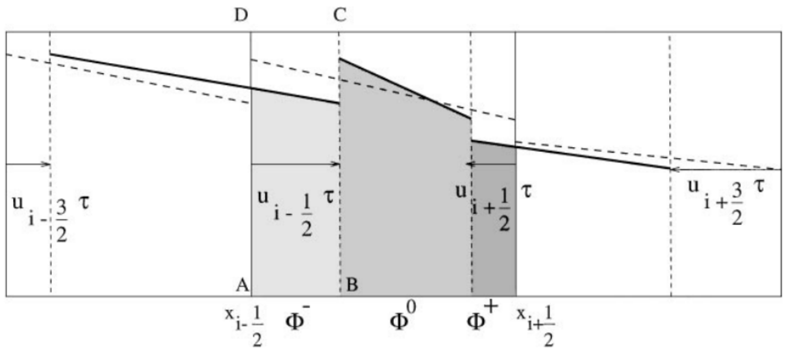

Figure 2.2: Lagrangian transport of the interface segments using the CIAM scheme, the image is reproduced with permission from Gueyffier et al. [14]. A 2D schemetic of the geometric calculation of the fluxes of the volume fraction field is shown, for the advection substep along the horizontal direction. The central cell (i, j, k) undergoes a net compression during this substep. The fluxes Φ^- , Φ^0 and Φ^+ are the volumes under the advected interface segments advected by the interpolated velocity field, intersected by the (i, j, k) cell boundaries.

where the compression coefficient $\overline{C}^{n,d}_{i,j,k}$ is simply equal to the value of the colour function $C^{n,d}_{i,j,k}$ at the start of the corresponding advection substep. Although the flux terms cancel upon integration throughout the whole domain, one can clearly see that the compression terms do not sum up to zero due to the changing prefactor in front of the directional divergences. This precise issue brings us to the next advection scheme.

Eulerian Implicit This advection scheme was developed by Weymouth and Yue [10] in order to specifically tackle the problem of discrete conservation when it comes to direction-split geometrical advection schemes [13] . The scheme fundamentally employs a forward Eulerian method in order to carry out temporal integration of the fluxes, with the fluxes themselves computed as the quantity of the substance entering or exiting a given control volume through its fixed surfaces, as shown in figure 2.3. This is in contrast with the flux computation method in the case of CIAM, where the interface segments are propagated forward in time in a Lagrangian fashion.

13: By 'discrete conservation' we mean that the sum of the directional divergences sum upto zero, to the accuracy of machine precision.

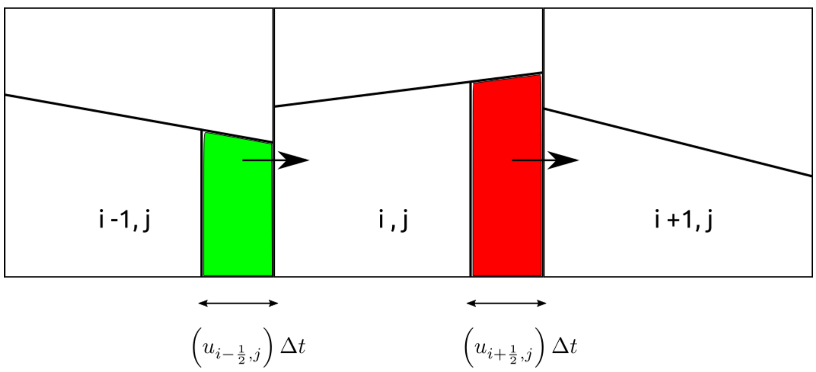

Figure 2.3: A 2D schemetic of the Eulerian (geometric) flux calculation using the Weymouth-Yue [10] scheme for the advection substep along the horizontal direction, with the interface reconstructed using the volume fraction field at the start of the substep. The colour fraction of the central cell (i, j) is updated during this substep through the addition of the fluxes (coloured regions), with the green polygon corresponding to the volume entering the cell i, j from the $i - 1, j$ and the red one corresponding to that exiting i, j into $i + 1, j$. The geometric flux calculations are made on the basis of the interfacial positions at the start of the substep, and the face centered velocities of the cell in question.

The subtle but important tactic used in this scheme lies in the manner in which the prefactor to the compression term [14] is treated, with its definition being :

14: Compression coefficient is used as a short-hand version of 'prefactor to the compression term'.

$$\overline{C}^{n,d}_{i,j,k} = H\left(C^{n,0}_{i,j,k} - 1/2\right) \tag{2.13}$$

where H is a one-dimensional Heaviside function. This renders the compression coefficient independent of the direction of the advection substep, consequently enabling the three discrete directional divergences to sum up to zero [15] Therefore, the scheme is able to demonstrate volume conservation, subject to local CFL restrictions [16] . To summarise, we can rewrite equation 2.10 for the Weymouth-Yue scheme as -

15: In numerical terms, we can only ensure that they sum up to the accuracy of the Poisson solver $\sim 10^{-3} - 10^{-6}$, with the limiting factor being the level of machine accuracy ($\sim 10^{-14} - 10^{-17}$).

16: For a proof of discrete volume conservation subject to certain CFL criteria, refer to the appendix of [10].

$$C^{n,d+1}_{i,j,k} = C \left[1 + \left(\frac{\Delta u_q}{\Delta x} \right)^{n,d}_{i,j,k} \right] - F^{n,d}_{+} (C) - F^{n,d}_{-} (C) \tag{2.14}$$

where C is a constant with a value of either 0 or 1, determined by the value of $C^{n,0}_{i,j,k}$ according to equation 2.13.

2.3 Time Marching

In order to describe the overall numerical algorithm for the one-fluid Navier-Stokes equations with variable density and viscosity, we choose to the reframe our equations in a more convenient operator form, as presented below :

$$\frac{\partial}{\partial t} \left(\rho \boldsymbol{u} \right) = L \left(\rho, \boldsymbol{u} \right) - \nabla p \tag{2.15}$$

The operator L in the above expression can be decomposed in an explicit fashion as :

$$L = L_{adv} + L_{\mu} + L_{\sigma} + L_{g} \tag{2.16}$$

where the L_{adv} represents the conservative advection, L_{μ} represents the diffusive forces generated by viscous stresses, L_{σ} represents the capillary forces arising from the surface tension model and finally L_g represents the volumetric (body forces) source term.

Spatio-temporal Discretization

We apply the spatially discretized versions of these operators (denoted by the superscript h) onto the primary variables ($C, \boldsymbol{u}$), and march forward in time using a small, possibly variable time-step τ such that $t_{n+1} = t_n + \tau$. We shall be dropping the subscript i, j, k from this point onwards, with the understanding that the operators in equation 2.16 apply uniformly to all control volumes. In the first part of the algorithm, the volume fraction field C^n is updated to the next timestep , with the superscript n signifying discretization in time. The operation can be written as follows -

$$C^{n+1} = C^n + \tau L_{vof}^h \left(C^n, \boldsymbol{u}^n\right) \tag{2.17}$$

The temporal evolution of the volume fraction field represented above by the operator L_{vof}^h is in accordance with the Lagrangian explicit or Eulerian implicit advection schemes, as described in the previous sections. Once we have obtained the updated field C^{n+1}, we can move on to the temporal update of our momentum field given by -

$$\begin{aligned}\rho^{n+1} \cdot \boldsymbol{u}^* = \rho^n \cdot \boldsymbol{u}^n + \tau L_{adv}^h \left(C^n, \boldsymbol{u}^n\right) + \\ \tau \left[L_\mu^h \left(C^{n+1}, \boldsymbol{u}^n\right) + L_\sigma^h \left(C^{n+1}\right) + L_g^h \left(C^{n+1}\right)\right]\end{aligned} \tag{2.18}$$

The advection operator L_{adv}^h is implemented as high-order spatial schemes coupled with a choice of non-linear flux limiters such as QUICK, ENO, WENO, Superbee, Verstappen, BCG, for regions of constant density [17] . For control volumes in the vicinity of the interface location, we revert to lower order schemes due to the sharp jumps in the material properties across the interface. The functionality of the operator L_{adv}^h near the interface is tighly coupled to that of L_{vof}^h from equation 2.17, so as to ensure consistency in the discrete advection of mass and momentum The details regarding this coupling shall be the focus of subsequent chapters, where it is covered in more depth.

17: These high-order spatial schemes are based on well established methods developed to deal with hyperbolic conservation laws, for more details refer to the studies of Leveque [15] and Sweby [16].

Pressure-Poisson Projection

The velocity field is evolved using a classical time-splitting projection method as described in the seminal work of Chorin [17], which involves predicting an 'intermediate' velocity field $\boldsymbol{u}^*$ as given by equation 2.18, followed by a correction step as follows -

$$\boldsymbol{u}^{n+1} = \boldsymbol{u}^* - \frac{\tau}{\rho^{n+1}} \nabla^h p^{n+1} \tag{2.19}$$

The discrete pressure field required to correct the intermediate velocity is determined by imposing the conservation of mass, which in our incompressible framework reduces to necessitating the resulting velocity field to be divergence-free (solenoidal) -

$$\nabla^h \cdot \boldsymbol{u}^{n+1} = 0 \tag{2.20}$$

Thus, combining equations 2.19 and 2.20, we are left with a variable coefficient Poisson equation for the pressure :

$$\nabla^h \cdot \left(\frac{\tau}{\rho^{n+1}} \nabla^h p^{n+1}\right) = \nabla^h \cdot \boldsymbol{u}^* \tag{2.21}$$

The default Poisson solver used in 'PARIS Simulator' to invert the elliptic operator appearing in eqn. 2.21 is a red-black Gauss-Seidel (GS) solver with overrelaxation [18] . There is also has an in-house implementation of a multigrid solver for structured grids with 2^n number of points per direction, utilizing a fully parallelized V-Cycle scheme [18]. Relaxation operations are applied starting from the finest to the coarsest first, and then from the coarsest to the finest, with the number of relaxation operations being a user-adjustable parameter. Having a native multigrid solver allows for an efficient solution of the Poisson equation without the necessity of having external libraries/pre-conditioners (e.g. HYPRE) installed on the system. When it comes to 'Basilisk', an atypical multigrid solver is implemented using a "half" V-cycle in order to deal with the spatial inhomogeity of the grid size arising due to adaptive mesh refinement. For more details regarding the differences between the multigrid solver of 'Basilisk' and the classical implementation of a multigrid, one can refer to [19] .

[18]: Briggs (1987), 'A Multi
SIAM'

[19]: Popinet (2003)
adaptive solver for t
ler equations in con

The whole set of operations described up to this point, constitutes a temporal integration scheme of the first-order, which can be expressed as -

$$\left(C^{n+1}, \boldsymbol{u}^{n+1}\right) = L_1\left(C^n, \boldsymbol{u}^n\right) \tag{2.22}$$

where L_1 is the operator consisting of all the steps described so far, applied to the primary fields C and $\boldsymbol{u}$. Therefore, a second-order time integration can easily be computed by using L_1 to get a first prediction -

$$\left(C^{**}, \boldsymbol{u}^{**}\right) = L_1\left(C^n, \boldsymbol{u}^n\right) \tag{2.23}$$

The superscript $**$ refers to our first order prediction of the primary variables. Therefore, the second-order estimate can be obtained via averaging -

$$\left(C^{n+1}, \boldsymbol{u}^{n+1}\right) = \frac{1}{2}\left[\left(C^{**}, \boldsymbol{u}^{**}\right) + L_1\left(C^{**}, \boldsymbol{u}^{**}\right)\right] \tag{2.24}$$

2.4 Source Terms

The detailed descriptions of the methods used in our numerical platforms to deal with surface tension, viscosity and body forces have already been carried out in [1, 2, 20], therefore we briefly touch upon certain aspects of the operators in question, in particular, their interaction with the volume fraction field.

Surface Tension

We use the Continuum Surface Force method (CSF) as our model for surface tension, coupled with height functions for curvature computation. The height functions used in our implementation were first introduced in [20] , subsequently tested, revised and improved in [21, 22]. In general, the height functions are used to compute the curvature field based on second-order finite differences applied to the heights. Although, in regions of poor interfacial resolution [18] , the method reverts to certain fallbacks, one of which is curve fitting instead of height functions. The resulting curvature field is coupled with a well-balanced discretization with respect to the discrete pressure gradient, with the same discretization stencil applied to the volumetric (body) force term as well.

18: These are regions where the local radius of curvature is comparable to the grid size

Viscous Diffusion

We use second-order spatial discretizations of the viscous stresses, using centered differences [19] . The (variable) dynamic viscosity is computed based on the volume fraction field via weighted arithmetic or harmonic averaging (equations 2.6). The temporal treatment of the viscous term can be either in explicit or semi-implicit fashion, , but in the context of the present study we will be sticking exclusively with the explicit version.

19: The exact implementation differs slightly between 'Basilisk' and 'PARIS Simulator'

Artificial Atomization : The Falling Raindrop

3

The focus of the present chapter shall be to take a closer look at the issues plaguing numerical methods that try to deal with flows entailing significant contrasts between the material properties of the two fluids. Arguably, the most common instances of such flows are those involving the interaction between air and water, primarily in the form of droplets and bubbles that play important roles in both natural and industrial processes. As for the numerical platform, we use 'PARIS Simulator' [1] to carry out our simulations on this topic. A flow configuration that combines the complexities of large density-ratios with the interaction between capillary, viscous and inertial stresses is that of a water droplet falling in the air under the influence of gravitational acceleration. The contents of the chapter are primarily derived from the recent investigations of the falling raindrop in Fuster et al. [23] , in which the author is a primary contributor.

1: Refer to [1] for a detailed exposition of the numerical methods implemented in 'PARIS Simulator.

3.1 Problem Setup

The problem is characterized by a combination of Reynolds, Weber and Bond numbers, the definitions of which are as follows :

$$We = \frac{\rho_g U^2 D}{\sigma} \quad , \quad Re = \frac{\rho_l U D}{\mu_g} \quad , \quad Bo = \frac{\left(\rho_l - \rho_g\right) g D^2}{\sigma} \tag{3.1}$$

The subscripts l and g represent liquid and gas phases respectively. In our particular numerical setup, $We \simeq 3.2$, $Re \simeq 1455$ and $Bo \simeq 1.2$, thus corresponding to that of a $3mm$ diameter raindrop (a relatively large one) falling in the air at an approximate terminal velocity of 8 m/s (interpolated from empirical data, refer to Gunn and Kinzer [24]). The parameters in the problem setup are given in Table 3.1, and the schematic diagram given in Fig. 3.1. The droplet is initially placed at the center of a cubic domain (3D), whose side is 4 times the diameter of the drop.

Table 3.1: Parameter values used in the simulation of a falling water droplet in air.

ρ_g (kg/m^3)	ρ_l (kg/m^3)	μ_g $(Pa\,s)$	μ_l $(Pa\,s)$	σ (N/m)	D (m)	g (m/s^2)
1.2	0.9982×10^3	1.98×10^{-5}	8.9×10^{-4}	0.0728	3×10^{-3}	9.81

In order to properly reproduce and analyse the dynamics of a relatively large drop (high Reynolds flow) such as in our case, the numerical method has to accurately resolve the thin boundary layers [2] , the interaction of such layers with the capillary forces and finally the non-linear feedback of the complex 3D vortical structures present in the wake behind the

2: Even for simulations with 60 points across the droplet diameter, the boundary layer has only by 3-4 cells across it.

droplet. Such an undertaking was attempted by Dodd and Ferrante [25], in which they managed to delineate the different regimes concerning the behavior of the wake behind the droplet, although at relatively lower Reynolds numbers (the maximum Reynolds tested was ≃ 500, whereas in our case it is ≃ 1500). Therefore, our objective behind the demonstration of this particular test case is *not* to develop a high fidelity model of a raindrop [3], but rather carry out a stringent evaluation of the robustness of our numerical method compared to ones that are not mass-momentum consistent. For such a low Weber number the capillary forces dominate and the droplet should remain intact, and definitely not undergo any subsequent atomization.

3: In the Dodd and Ferrante [25] study , a droplet was allowed to fall from rest along a domain with a length corresponding to 32 times the droplet diameter, therefore necessitating a problem size of approximately 260 million cells.

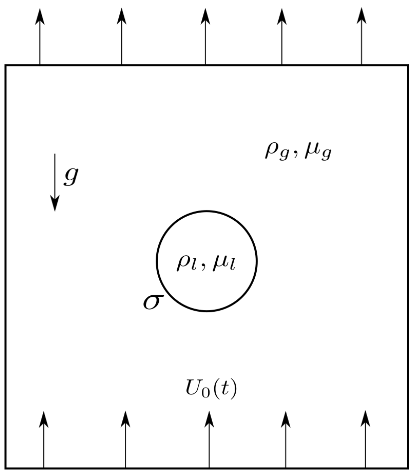

Figure 3.1: A 2D schematic of the numerical setup for the falling raindrop. A droplet of diameter D is placed at the center of a cubic domain of side L and $L/D = 4$. The liquid properties (ρ_l , μ_l) correspond to that of water, and the gas properties (ρ_g,μ_g) correspond to that of air. We apply a uniform inflow velocity condition with $U_0(t)$ and an outflow velocity condition at the top which corresponds to zero normal gradient. Boundary conditions on the side walls correspond to those of impenetrable free slip (no shear stress).

3.2 Numerical Instabilities

Numerical simulations of this configuration at moderate resolution [4] carried out with the standard version [5] of our numerical method results in the catastrophic deformations of the droplet as illustrated in Fig. 3.5, which we describe as 'fictitious' or 'artificial' atomization.

4: Droplet resolutions between $D/h = 16$ to $D/h = 64$ are considered to be moderate, where D is the droplet diameter and h is the grid size.

5: The standard version is based on the non-conservative formulation of the Navier-Stokes equations, concomitantly not ensuring consistency between discrete mass and momentum transport.

Instability Mechanism

We propose the following explanation in order to account for such numerical artifacts. To start with, we neglect gravity and viscous effects at this relatively large Reynolds number. Also, we are interested in steady-state flow [6]. On the axis and near the hyperbolic stagnation point at the front of the droplet one has $u_2 = 0$ for the transverse (radial) velocity and for the axial momentum balance

6: As the simulation starts with uniform flow in the gas and a zero velocity in the drop, there is a sudden large acceleration in the gas, resulting in the development of a dipolar velocity field akin to that of potential flow around a cylinder (sphere).

$$u_1 \partial_1 u_1 = -\frac{1}{\rho} \partial_1 p. \tag{3.2}$$

Due to the large viscosity and density ratios, it is not possible for the air flow to immediately entrain the water, so the fluid velocity is significantly smaller inside the droplet. In the air the acceleration near the stagnation point is of the order U^2/D, whereas the pressure gradient is

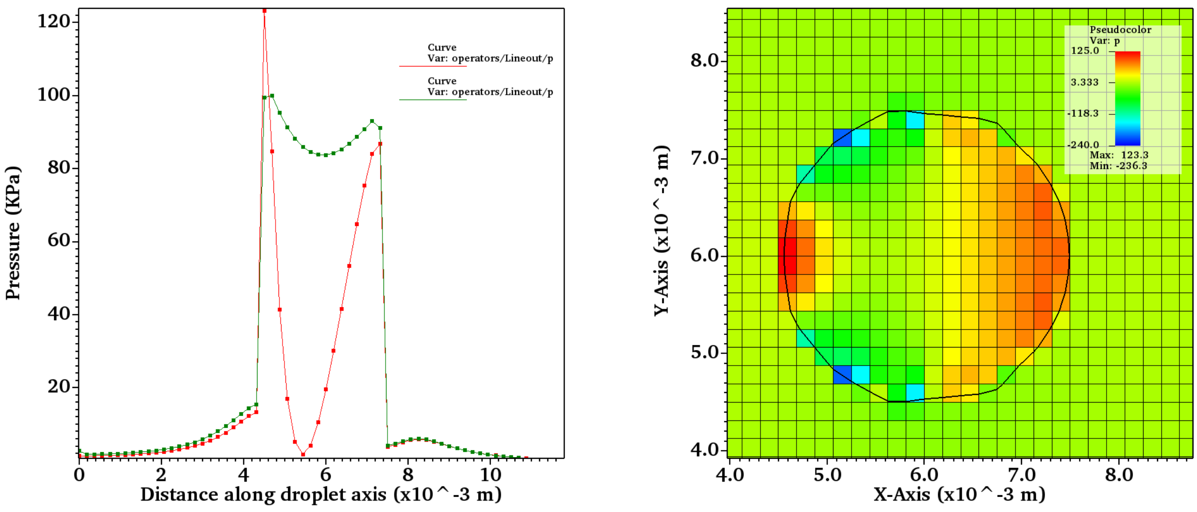

(a) (b)

Figure 3.2: The origin of the pressure peak in the front of the droplet. (a) The profile of the pressure on the axis a few timesteps after initialisation with the standard, non-consistent method (red curve) and the consistent method based on the conservative Navier-Stokes formulation (green curve). Much larger pressure gradients are present across the interface using the non-consistent method. (b) The pressure distribution immediately after the start of the simulation using the standard, non-consistent method. The pressure peak has not yet resulted in the formation of a dimple. In all figures the droplet resolution corresponds to $D/h = 16$. The simulations are carried out with the CIAM advection method, in conjunction with the Superbee limiter.

$$\partial_1 p \sim \rho_g U^2/D. \tag{3.3}$$

The pressure gradient in the liquid is much smaller, however, in the case of a mixed cell the water density multiplies with the gas acceleration U^2/D, so that

$$\partial_1 p \sim \rho_l U^2/D, \tag{3.4}$$

then a large pressure gradient results in the mixed cell or cells. This large pressure gradient results in a pressure spikes inside the droplet near the front stagnation point, as shown in Figure 3.2. Such pressure gradients are balanced by surface tension only for a sufficiently large curvatures near the droplet front. This explains the presence of a “dimple” often observed in low resolution simulations of the falling drop. This artifact had been observed by Xiao [26] in a similar case [7] involving the sudden interaction of a droplet at rest with a uniform gas flow. The resulting large un-physical pressure gradients across the interface eventually lead to its rapid destabilization and concomitant breakup.

7: In the thesis of Xiao, the focus was on the analysis of droplet breakup corresponding to different Weber number regimes.

Visualization of the flow around the droplets (Figure 3.4) illustrates the challenging nature of the flow configuration, even for such a seemingly simple physical problem. As one can observe, the boundary layers are extremely thin. Therefore, even though the velocity field is continuous across the interface (in the discrete sense) in the absence of mass transfer,

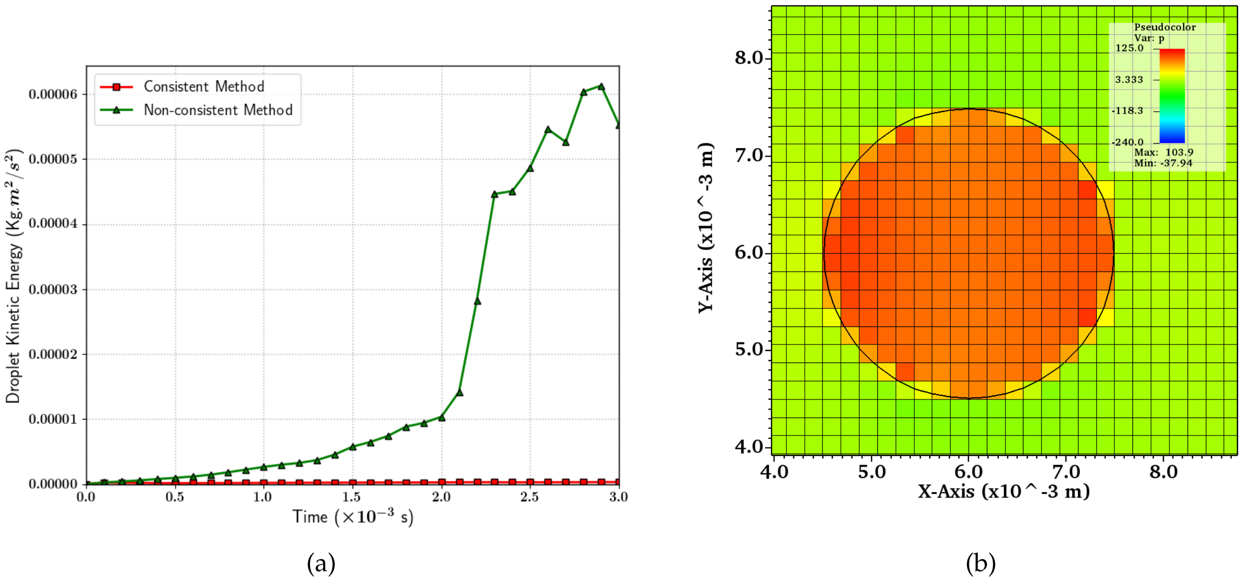

Figure 3.3: (a) Comparison of the temporal evolution of droplet kinetic energy. The standard non-consistent method displays spikes in the kinetic energy that are approximately 3 orders of magnitude larger than that of the consistent method, leading to rapid destabilization. (b) The pressure distribution immediately after the start of the simulation using the consistent method (based on a conservative Navier-Stokes formulation). In all figures the droplet resolution corresponds to $D/h = 16$. The simulations are carried out with the CIAM advection method, in conjunction with the Superbee limiter.

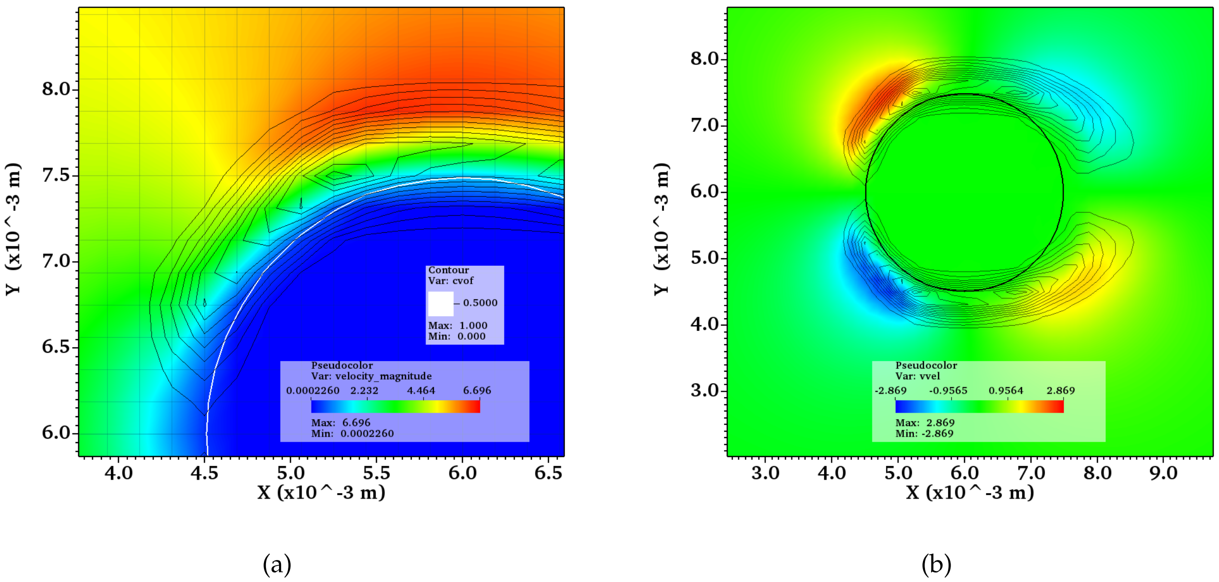

Figure 3.4: Flow field around the $3mm$ droplet with $D/h = 16$ immediately after the start of the simulation with the consistent method, demonstrating the contours of the norm of the vorticity field (black lines) . The 2D cross-section in these figures corresponds to the mid-plane slice along the Z axis, where the inflow is along the X axis and gravity opposite to it. (a) The velocity magnitude. As one can observe, the boundary layer is resolved by only 2-3 cells. (b) The velocity component in the Y direction, perpendicular to the flow. As the flow develops further, a marked separation of the boundary layers is observed with a more complex vortical region in the wake. The figures correspond to simulations carried out with the CIAM advection method, in conjunction with the Superbee limiter.

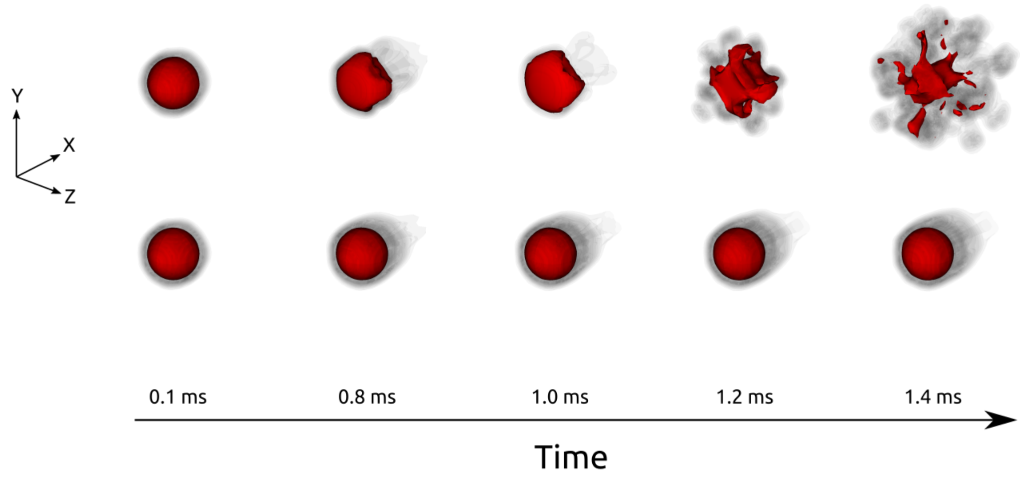

Figure 3.5: A comparison of the temporal evolution between the standard non-consistent method (top row) and the consistent method based on the conservative formulation of the governing equations (bottom row), using the combination of CIAM advection scheme coupled with the Superbee flux limiter. The flow is along the positive X direction, with gravity along the opposite direction. The red contour indicates the isosurface of the volume fraction field corresponding to a value of 0.5, whereas the black contours surrounding the drop represent isosurfaces of the magnitude of vorticity. The raindrop with the non-consistent method displays massive deformations leading to artificial breakup as a result of rapidly growing numerical instabilities. The droplet resolution for both methods is $D/h = 16$.

there is the appearance of strong velocity variations at the scale of the grid size for such coarse levels of grid refinement.

3.3 Stabilization Strategies

The cascading nature of the numerical instabilities that lead to the eventual (un-physical) fragmentation of droplet is not just a cause of concern in the context of modeling a raindrop, but it has important implications within the more broader scope of atomization and other complex fragmentation phenomena.

Primary Concern

Arguably, the most important objective of numerical investigations of physical phenomena involving fragmentation is the quantification of the size of the features that result from a series of topological changes [8] . A typical example is the statistical distributions of drop sizes, where the drops are generated via some fragmentation mechanism. [9] As demonstrated in the present studies using the standard non-consistent method, the artificially atomized drop leads to the generation of a large number of smaller fragments, which if counted, will skew the resulting droplet size distributions towards the smaller sizes. Therefore, the falling raindrop serves as a faithful representation of the numerous under-resolved features that are typically omnipresent in numerical studies of complex fragmentation phenomena. The inability to discern between the drops resulting from physically consistent mechanisms and those that result from 'numerical fragmentation' is exactly why there is a need to develop numerical schemes that circumvent the occurrence of such numerical instabilities.

8: In the context of surface tension dominated flows, these features are primarily drops and bubbles, occassionally one can also be interested in transient features such as thin sheets, ligaments etc.

9: These are generally in the form of probability density functions (PDF).

Consistent Mass-Momentum Transport

The most common and brute force approach that one can apply in order to suppress or circumvent such numerical instabilities is by using a combination of extremely refined meshes coupled with larger domains [10] A more computationally efficient approach would be to use a conservative formulation [11] of the Navier-Stokes equations, in order to achieve consistency in the discrete transport of mass and momentum. In this section, we shall take a closer look at how the utilisation of the consistent method enables us not only to stabilize majority of the numerical instabilities we have come across, but also delivers relatively good approximations of the flow dynamics involved. A thorough and detailed exposition of the principles behind the consistent method and the different strategies towards achieving consistent transport is covered in the ensuing chapter.

10: In the study of Dodd and Ferrante [25], a computational domain with length corresponding to 32 times the diameter is employed, resulting in a problem size of approximately 260 million cells, that too for a relatively low Reynolds number.

11: A prerequisite of methods that use consistent mass-momentum transport is the formulation of the convective operators in the conservative manner i.e divergence of fluxes instead of gradients of the primary (discontinuous) variables.

We observe that applying the method that ensures consistent mass-momentum transport brings a considerable and systematic improvement over a spectrum of different flux limiters (WENO, ENO, Superbee, QUICK, Verstappen) and CFL numbers, as evidenced by comparing the figures 3.2 and 3.3. To summarize, the simulations broadly fall into three categories. The first two categories concern those that use the method ensuring consistent mass-momentum transport, and as a result maintain physical values of the kinetic energy and smooth interface shapes. Certain simulations amongst the ones carried out with this consistent method display some numerical instabilities (but not leading to catastrophic deformation) [12] resulting due to the particular choice of the advection scheme (CIAM/WY) and flux limiter (QUICK/WENO/ENO/Superbee/Verstappen) combination.

12: This may be due certain issues regarding the treatment of outflow boundary conditions in our numerical platform 'PARIS Simulator'.

Finally, in the third category are the simulations carried out with the standard non-consistent method that rapidly blow up, displaying marked peaks or spikes in kinetic energy as a function of time, associated with massively deformed interface shapes (see figure 3.5). Additionally, our studies suggest that certain combinations of the advection scheme and the flux limiter are numerically more robust than others [13] , in particular, the most stable combinations are that of CIAM advection with Superbee limiter, and the WY advection with QUICK limiter.

13: Further detailed investigations are required to understand the difference in code stability as a function of the choice of flux limiter and advection scheme combination.

We illustrate the performance of the consistent method through the results of our simulations in Figure 3.7. The spatial resolutions correspond to $D/h = 8, 16, 32$ and 64 using the WY advection scheme in combination with the QUICK flux limiter, while keeping the same value for the inflow velocity boundary condition. The quantities of interest while examining the robustness of the method are the temporal evolution of the droplet kinetic energy (Fig. 3.7. (a)) and the moment of inertia of the droplet along the three directions (Fig. 3.7. (b),(c),(d)) . The inflow is along the X direction with gravity opposite to it. The moment of inertia is used as a descriptor of the 'average' droplet shape, with the three moments of inertia along the different axes I_m defined as -

$$I_m = \int_{\mathcal{D}} H x_m^2 d\boldsymbol{x} \quad , \quad \text{where,} \quad 1 \leq m \leq 3 \tag{3.5}$$

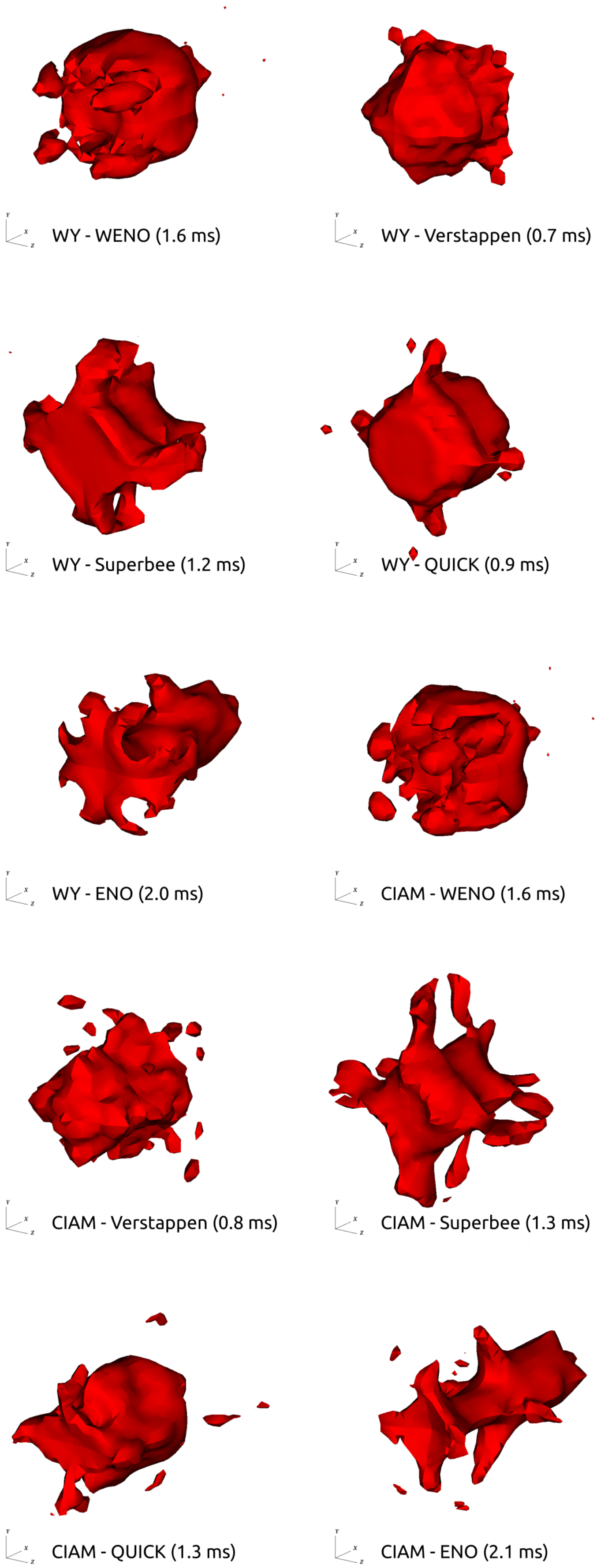

Figure 3.6: A juxtaposition of the different manifestations of 'artificial' atomization one encounters while using the standard method that does not involve consistency between the discrete transport of mass and momentum. The red contours indicate the isosurface of the volume fraction field corresponding to a value of 0.5, acting as a good proxy for the exact interfacial position. One can clearly observe that the un-physical fragmentation of the raindrop is symptomatic of the non-consistent method, systematically across all combinations of flux limiters and advection schemes. The symbol "WY" in the legend corresponds to those run using the Weymouth-Yue advection scheme, and "CIAM" corresponds to the CIAM scheme. Brief descriptions of these advection schemes can be found in the preceding chapter 2. The implementation of the non-linear flux limiters i.e WENO, ENO, QUICK, Superbee, Verstappen correspond to that of well established methods developed to deal with hyperbolic conservation laws, for more details refer to the studies of Leveque [15] and Sweby [16]. The time stamps are indicative of the moments at which the interface is the most deformed, and do not necessarily correspond to the moment at which the code crashes.

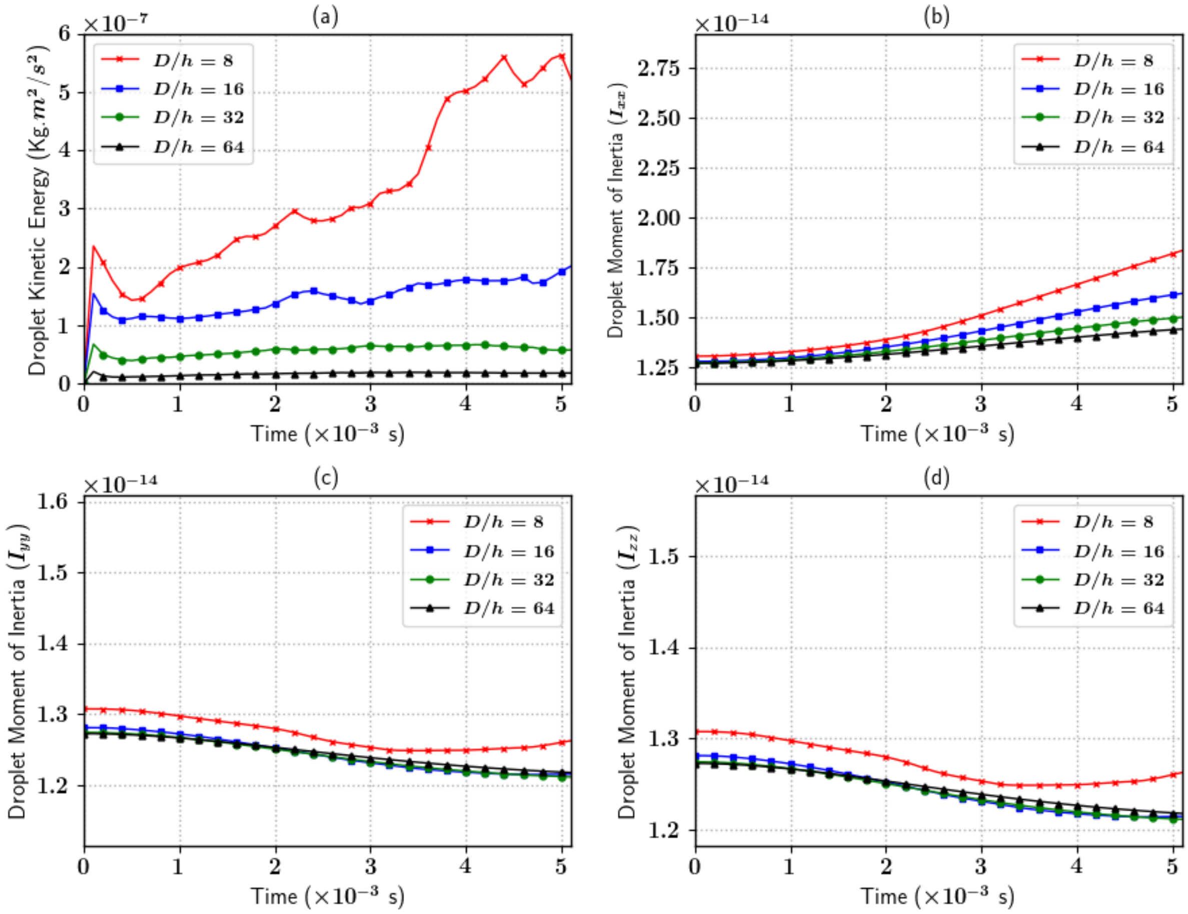

Figure 3.7: Temporal evolution of quantities of interest to evaluate the performance of the consistent scheme for different spatial resolutions. (a) Kinetic energy of the droplet. (b) Moment of inertia of the droplet along the flow (X) direction. (c) and (d) Moment of inertia of the droplet along the directions perpendicular to flow (Y,Z), evolution of I_{yy} seems to be more or less identical to I_{zz}.

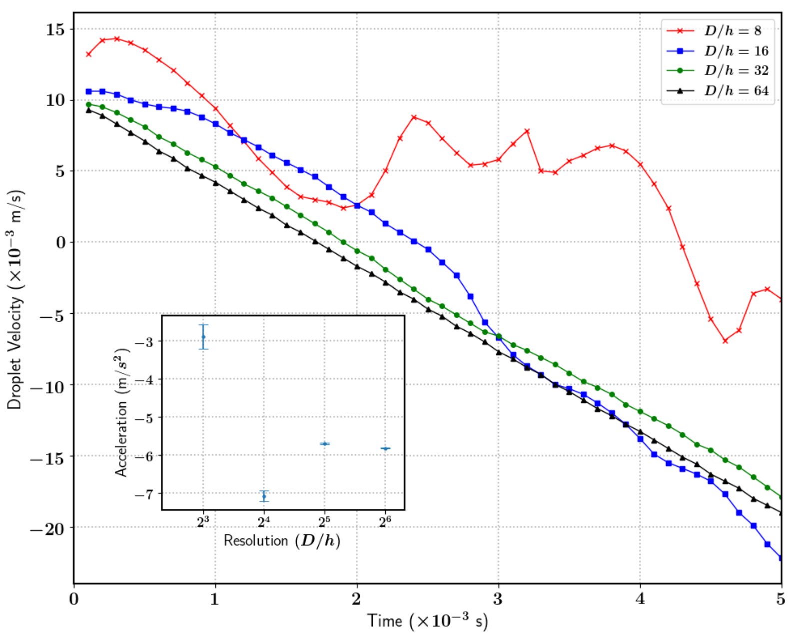

Figure 3.8: Comparison of droplet velocity as a function of time, for different droplet resolutions. The simulations were carried out with the consistent version of our method, using the combination of the WY advection scheme with the QUICK limiter. The droplet velocities correspond to that of their respective center of masses. Inset : Convergence of the droplet acceleration as a function of resolution, computed using the best linear fit over the temporal variation of their respective velocities. The error bars signify the asymptotic standard error (least-squares) corresponding to the obtained linear fits.

where $\mathcal{D}$ is the computational domain and x_m is the distance of the interface relative to the center of mass of the droplet. The kinetic energy of the droplet evolves in a relatively smooth manner, without the presence of sudden spikes and falls which are emblematic of the standard non-consistent method (refer to Fig. 3.3). Such abrupt changes in kinetic energy of the droplet have been found to be associated with instants when the droplet undergoes 'artificial' atomization or breakup, henceforth resulting in the catastrophic loss of stability for the numerical method. We observe a systematic drop in the amount of the droplet kinetic energy as we increase resolution, with the most probable explanation being that of the suppression of spurious interfacial oscillations which are rampant at lower resolutions. There is also a component of the kinetic energy of the droplet associated with the internal coherent vortical structures generated due to the interaction of aerodynamic shear at the interface, evidenced by the non-zero value of the kinetic energy even for the most highly resolved droplets. Finally, the moment of inertia of the droplet appears to evolve in a smooth manner for all droplet resolutions, with higher resolutions exhibiting lower amounts of inertia as a result of the more compact shapes obtained once the spurious interfacial deformation modes are subdued. This observation holds true for the moment of inertia curves regardless of direction.

We have to keep in mind that the velocity inflow condition does not correspond to the 'exact' teminal velocity field an actual falling raindrop might experience, hence the droplet in our numerical setup does have some finite acceleration due to the imbalance between the aerodynamic forces and gravity. In Figure 3.8, we demonstrate the velocity of the center of mass of the droplet (in the frame of reference of the box enclosing the droplet) as a function of time, and its behavior as we increase the droplet resolution. As one can observe, due to the imbalance of forces acting on the droplet, it undergoes a net acceleration as evidenced by the approximately linear increase (absolute value) in the velocity as a function of time. The temporal variation in the droplet velocity is fitted to a linear polynomial in order to evaluate the droplet acceleration by means of a standard least-squares approach, for each droplet resolution. We illustrate (inset Figure 3.8) that we achieve more accurate fits as a consequence of higher droplet resolutions, as evidenced by a decrease in the standard error on the fits ranging from $\pm 11.1\%$ for $D/h = 8$ to a value of $\pm 0.12\%$ for the highest resolution of $D/h = 64$. The results obtained in this section indicate that especially when it comes to low resolutions, our numerical method can be used to get relatively good estimates of the underlying flow features of the droplet without observing an un-physical evolution as a consequence of discretization errors.

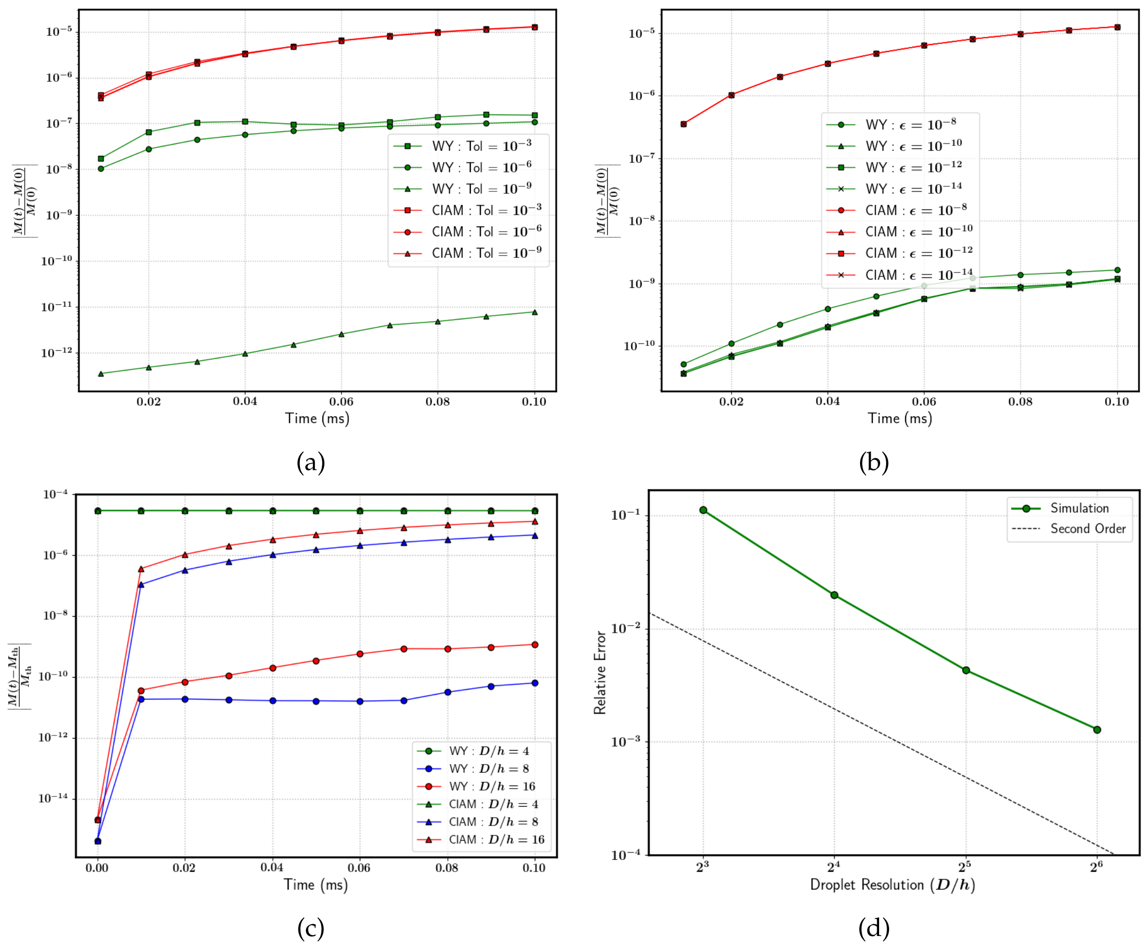

Figure 3.9: Relative change in the mass of the droplet as a function of time in plots (a), (b) and (c). The simulations are carried out with a resolution of $D/h = 16$, for a total time of 0.1 milliseconds. The symbol "WY" in the legend corresponds to those run using the Weymouth-Yue advection scheme in combination with the QUICK limiter, and "CIAM" corresponds to the CIAM scheme in combination with the Superbee limiter. (a) The dependence of the mass conservation properties of the scheme as a function of the Poisson solver tolerance is tested. For the WY-QUICK combination, using a stricter tolerance results in better mass conservation, whereas the conservation properties of the CIAM-Superbee combination seems to be independent of the tolerance. (b) Dependence of the mass conservation on the clipping parameter employed. The CIAM-Superbee combination again seems to be impervious to changes in clipping, whereas WY-QUICK seems to perform slightly better by lowering the parameter. (c) Dependence of the mass conservation properties on the droplet resolution. The WY-QUICK combination displays better results for all except the lowest resolution. (d) Variation of the relative error from the least-squares fit on the droplet acceleration, in the frame of reference of the static box. The corresponding droplet accelerations are plotted in the inset of figure 3.8. The reduction in the relative error follows roughly second-order spatial convergence.

Consistent Mass-Momentum Transport 4

The stability of numerical methods that attempt to model interfacial flows involving large density contrasts face several challenges, key amongst them being the transport of mathematical discontinuities that arise from the contrast in the material properties of the fluids involved. Extremely small numerical errors are ubiquitous as a consequence of the numerous approximations involved at each and every step of the algorithm [1] . In the context of such flows, such errors generally result in physically inconsistent mass and momentum transfer across the interface, often from the denser phase towards the lighter phase. The presence of large density or viscosity contrasts tend to amplify the growth of these cascading numerical errors, eventually leading to significant (often catastrophic) interfacial deformations followed rapidly by a loss of numerical stability. In this chapter, we present a detailed exposition of our class of numerical methods which are designed specifically to circumvent or suppress the growth of such numerical instabilities when dealing with flows entailing large density-ratios. The implementations of the numerical algorithms are developed for finite volume discretizations using uniform Cartesian grids in 3D, on the 'PARIS Simulator' [1] numerical platform. Some contents of the chapter are primarily derived from the recent study by Fuster et al. [23] , in which the author is a primary contributor.

1: Approximations are made while interfacial propagation , curvature computation, surface tension modeling etc.

[23]: Fuster et al. (2018), 'A momentum-conserving, consistent, Volume-of-Fluid method for incompressible flow on staggered grids'

4.1 General Principles

In the past two decades, considerable efforts have been made in the design of numerical methods to deal with large density-ratios. The underlying principle behind these endeavours is that the governing equations for the transport of mass and momentum are modeled using a conservative formulation (divergence of fluxes), instead of standard non-conservative forms which themselves were adapted directly from techniques developed originally for single-phase flows. This formulation enables one to render the discrete transport of momentum *consistent* with respect to the discrete transport of mass [2] . Such a tight coupling of the propagation of errors between the discrete mass and momentum fields enables alleviation of many of the issues that plague such numerical methods, especially in the context of low to moderate spatial resolutions. A secondary but important mitigating factor is the advancements made in the modeling of capillary forces, resulting in the adoption of consistent and *well-balanced* surface tension formulations. [3] . We refer the reader to influential works of Popinet [6, 20] to get a better understanding of the issues surrounding surface tension implementations.

2: First of all, the transport of mass (density) has to be made consistent with that of the geometric transport of volume fraction.

3: Consistency in the context of surface tension models refers to the ability of methods to progressively achieve more accurate estimations of interfacial curvature as a result of increasing spatial resolution, whereas well-balanced refers to the ability to recover certain static equilibrium solutions pertaining to surface tension dominated flows without the perpetual presence of parasitic or spurious currents in the velocity fields.

Major Iterations in Literature

The first study to address the issue of consistency between mass and momentum transport was the seminal work of Rudman [27] . The fundamental hurdle in the implementation of mass-momentum consistent transport for staggered configurations of primary variables (pressure and velocity) is the inherent difficulty in reconstructing mass (defined on centered control volumes) and its corresponding fluxes onto the staggered control volumes on which momentum is defined. Rudman introduced the strategy of carrying out mass advection [4] on a grid twice as fine as that of momentum, thereby enabling a 'natural' and intutive way to reconstruct mass and its fluxes onto staggered momentum control volumes. However, the method uses a VOF based convolution technique for curvature computation, which is neither consistent nor well-balanced.

[27]: Rudman (1998), '
method for incompress
with large density vari

4: Mass advection was carried out using using algebraic flux reconstructions.

Bussmann et al. [28] were able to circumvent the issue surrounding staggered grids altogether by using a collocated arrangement in the context of hexahedral unstructured meshes, coupled with an unsplit Eulerian flux computation method. The study though makes no mention of any surface tension model.

[28]: Bussmann et al. (2002), 'Modeling high density ratio incompressible interfacial flows'

Level set based methods in the context of mass-momentum consistent transport were implemented first by Raessi and Pitsch [29] , followed by Ghods and Hermann [30]. In the former, the consistency problem is tackled by means of a semi-Lagrangian approach, computing geometric level set derived fluxes at two different time intervals, whereas in the latter, a collocated arrangement is used. Nonetheless, both methods face certain drawbacks, notably the applicability only to 2D in case of Raessi and Pitsch, as well as a lack of well-balanced surface tension models for both these methods.

[29]: Raessi et al. (2012),
and momentum transpo
incompressible interfaci
density ratios using the

Recent advances concerning volume-of-fluid based methods that employ unsplit (conservative) geometric flux reconstructions were made by LeChenadec and Pitsch [31] , and later by Owkes and Desjardins [32]. LeChenadec and Pitsch utilize a Lagrangian remap method in order to construct consistent mass-momentum fluxes for the staggered control volumes, while Owkes and Desjardins use mass advection on a doubly refined grid (same principle as Rudman) to achieve consistency. Although [31] implements a well-balanced surface tension model, the VOF convolution based curvature computation is not consistent. In case of [32] , they use mesh-decoupled height functions to compute curvature while coupling it with a well-balanced surface tension model. However, their semi-Lagrangian flux computation procedure involving streak tubes and flux polyhedra are extremely convoluted in 3D.

[31]: Le Chenadec et al. (2013), 'A monotonicity preserving conservative sharp interface flow solver for high density ratio two-phase flows'

[32]: Owkes et al. (2017), 'A mass and momentum conserving unsplit semi-Lagrangian framework for simulating multiphase flows'

Certain methods attempt to combine the qualities of both VOF and level set methodologies (CLSVOF), as proposed in the works of Vaudor et al. [33] , and more recently by Zuzio et al. [34]. They both tackle the consistency issue by means of projecting the direction-split geometric fluxes onto a twice finer grid, which are subsequently recombined to reconstruct consistent fluxes for mass and momentum for the staggered control volumes. This approach allows them to bypass the requirement of conducting mass advection on a twice finer grid (as in the original Rudman method), thereby deriving the benefits of a sub grid without the

[33]: Vaudor et al. (2017), 'A consistent mass and momentum flux computation method for two phase flows. Application to atomization process'

added computational cost of doubly refined mass transport. In addition, both Vaudor et al. [33] and Zuzio et al. [34] adopt well-balanced surface tension models with consistent level set based curvature estimation. However, the purported advantages of both these methods with regards to reduced computational costs is not quite evident, as additional complexities are introduced due to the projection (reconstruction) of fluxes onto a the twice finer mesh, which would not be necessary in the first place if mass transport had been carried out on the twice finer mesh itself.

[34]
mon
for h
com

Patel and Natarajan [35] developed a hybrid staggered-collocated approach to solve the consistency issue on polygonal unstructured meshes, complemented with a well-balanced surface tension model. Nevertheless, the VOF advection is based on algebraic transport, not to mention the use of a VOF convolution based curvature computation, which is inherently not consistent.

[35]: Patel et al. (2017), 'A novel consistent and well-balanced algorithm for simulations of multiphase flows on unstructured grids'

More recently, Nangia et al. [36] developed a CSLVOF method for dynamically refined staggered Cartesian grids. They utilize Cubic Upwind Interpolation (CUI) schemes to reconstruct consistent mass and momentum fluxes on the staggered control volumes, using the information from the additional mass advection equation they solve alongside the level set function. However, the reconstruction of mass fluxes using CUI schemes are inherently algebraic, with their comparative advantage against fluxes computed via geometric constructions being an open question [5] .

[36]: Nangia et
compressible Na
density ratio mu

5: refer to Mirjalili et al. [11].

To get a bird's eye view of the numerous features employed by the methods in existing literature, we refer the reader to tables which respectively provide systematic overviews of the VOF based and level set based approaches.

Our Approach

In the present body of work, we start by precisely defining the essential (desired) attributes of a numerical scheme that ensures discrete consistency between mass and momentum transport :

- The discontinuity of the mass (volume fraction derived density field) should propagate at the exact 'numerical' speed as that of the discontinuity of the momentum field.
- The numerical transport of momentum should be performed in a manner consistent to the transport of mass for each direction, implying that the momentum fluxes must be obtained directly from geometrically computed fluxes of mass (volume).

In order to tackle the challenge of consistent transport on staggered control volume configurations, we have developed two different strategies, namely, the *shifted fractions* method and the *sub-grid* method. The former uses geometrical reconstructions to derive a *shifted* volume fraction field which is centered on the staggered control volumes, whereas the latter adopts the Rudman [27] strategy of volume advection on a twice finer grid in order to enable consistent reconstruction of mass and momentum on the staggered control volumes. Another key contribution of this body of work is to extend the conservative direction-split mass transport algorithm of Weymouth and Yue [10] to the direction-split transport of momentum.

A thorough description of the shifted fractions method is can be found in the recent study by Fuster et al. [23] , and a detailed exposition of the sub-grid method is currently under preparation at the time of writing. We shall be taking a closer look at these two stratetgies in the upcoming sections.

[10]: Weym volume-of- simulation

[23]: Fust conservin method fo gered gric

4.2 Basic Expressions

We start with the advection of the interface position, which in the VOF framework is given by -

$$\frac{\partial H}{\partial t} + \nabla \cdot (\boldsymbol{u} H) = H\ (\nabla \cdot \boldsymbol{u}) \tag{4.1}$$

In the VOF approach, the approximation to the interface Heaviside function contains a sharp discontinuity, in contrast to the level set approach where the approximation is continuous in the discrete sense.

Integrating this equation in time after carrying out spatial discretization, one obtains -

$$C^{n+1}_{i,j,k} - C^{n}_{i,j,k} = -\sum_{\text{faces } f} F^{(c)}_f + \int_{t_n}^{t_{n+1}} \mathrm{d}t \int_{\Omega} H\ (\nabla \cdot \boldsymbol{u})\ \mathrm{d}\boldsymbol{x}\,, \tag{4.2}$$

$C^n_{i,j,k}$ is the colour function or volume fraction field at time step n obtained through the finite volume discretization of the interface Heaviside function.

where the first term on the right-hand side is the summation over the cell faces f of the fluxes $F^{(c)}_f$ [6] . As one can clearly observe, the "compression" term on the right-hand side of equation (4.1) disappears for incompressible flow, however it is essential in the context of direction-split geometric advection schemes. The definition of the geometric fluxes in mathematical form is -

6: These fluxes of $(\boldsymbol{u}H)$ are computed via geometrical reconstructions, and not via high-order non-linear interpolation schemes which are the standard (in the absence of discontinuities) .

$$F^{(c)}_f = \int_{t_n}^{t_{n+1}} \mathrm{d}t \int_f u_f(\boldsymbol{x}, t) H(\boldsymbol{x}, t)\, \mathrm{d}\boldsymbol{x}\,, \tag{4.3}$$

where $u_f = \boldsymbol{u} \cdot \boldsymbol{n}_f$ [7] . Once an approximation for the evolution of $(\boldsymbol{u}H)$ during the time step is chosen, a four-dimensional integral remains to be computed in equation (4.3). The advection schemes used are CIAM and Weymouth-Yue, which have been described briefly in chapter 2.

7: Component of the velocity normal to the control surface f.

Directional splitting results in the breakdown of equation (4.2) into three equations, one for each advection substep -

$$C^{n,l+1}_{i,j,k} - C^{n,l}_{i,j,k} = -F^{(c)}_{m-} - F^{(c)}_{m+} + c_m \partial^h_m u_m\,, \tag{4.4}$$

After each advection substep (4.4), the interface is reconstructed with the updated volumes $C^{n,l+1}_{i,j,k}$, then the fluxes $F^{(c)}_f$ are computed for the next

The superscript $l = 0, 1, 2$ is the substep index, i.e. $C^{n,0}_{i,j,k} = C^{n}_{i,j,k}$ and $C^{n,3}_{i,j,k} = C^{n+1}_{i,j,k}$. The face with subscript $m-$ is the "left" face in direction m with $F^{(c)}_{m-} \geq 0$ if the flow is locally from right to left. A similar reasoning applies to the "right" face $m+$.

substep. Importantly, we have approximated the compression term in (4.2) by -

$$\int_{t_n}^{t_{n+1}} \mathrm{d}t \int_{\Omega} H \partial_m u_m \mathrm{d}\boldsymbol{x} \simeq c_m \partial_m^h u_m \tag{4.5}$$

On the right hand sides of (4.4) and (4.5) the flux terms $F_f^{(c)}$ and the partial derivative $\partial_m u_m$ must be evaluated using identical discretized velocities. The expression $\partial_m^h u_m$ is a finite volume approximation of the spatial derivative corresponding to the mth component of the velocity vector along direction m, and the "compression coefficient" c_m approximates the color fraction. Its exact expression is dependent on the advection method [8] and it also entails the desirable property of C-bracketing [9]. Due to the possible dependence of the compression coefficient c_m on the Cartesian direction corresponding to the advection substep, the sum $\sum_m c_m \partial_m^h u_m$ may not necessarily vanish even if the flow is incompressible. As mentioned previously in chapter 2, the main appeal of the Weymouth-Yue method is its ability to keep this sum to zero, within the limits of machine precision.

There is no implicit summation carried out over m, and the superscript h denotes the spatial discretization of the operator.

8: Refer to chapter 2 to see the difference in the definitions of the compression coefficient between the CIAM and Weymouth-Yue methods.

9: The preservation of $0 \leq C_{i,j,k} \leq 1$ is referred to as C-bracketing.

Advection of Conserved Scalars

In order to achieve consistent transport of the discontinuous fields of mass and momentum, we start by trying to understand the advection of a generic *conserved* scalar quantity ϕ by a continuous velocity field -

$$\frac{\partial \phi}{\partial t} + \nabla \cdot \left(\phi\, \boldsymbol{u}\right) = 0 \tag{4.6}$$

where the field ϕ is smoothly varying except at the interface position, where it may be discontinuous. The essence of this study lies in the search of a scheme that propagates this discontinuity (ϕ) at the same speed as that of the advection of volume fraction (C).

Temporal integration of the spatially discretized version of (4.6) gives us -

The smoothness of the advected quantity away from the interface is verified for fields such as density ρ, momentum $\rho\boldsymbol{u}$ and internal energy ρe.

$$\phi_{i,j,k}^{n+1} - \phi_{i,j,k}^{n} = -\sum_{\text{faces } f} F_f^{(\phi)} \tag{4.7}$$

where the fluxes are defined as -

The sum on the right-hand side is the sum over faces f of cell i, j, k of the fluxes $F_f^{(\phi)}$ of ϕ, which are defined as the color function fluxes $F_f^{(c)}$ in (4.3).

$$F_f^{(\phi)} = \int_{t_n}^{t_{n+1}} \mathrm{d}t \int_f u_f(\boldsymbol{x}, t)\, \phi(\boldsymbol{x}, t)\, \mathrm{d}\boldsymbol{x} \tag{4.8}$$

In order to "extract" the discontinuity we introduce the interface Heaviside function $H(\boldsymbol{x}, t)$

$$F_f^{(\phi)} = \int_{t_n}^{t_{n+1}} \mathrm{d}t \int_f \left[u_f \, H \, \phi + u_f \, (1 - H) \, \phi \right] \, \mathrm{d}\boldsymbol{x} \tag{4.9}$$

Therefore, the flux can be decomposed into two components as -

$$F_f^{(\phi)} = \bar{\phi}_1 \int_{t_n}^{t_{n+1}} \mathrm{d}t \int_f u_f \, H \, \mathrm{d}\boldsymbol{x} + \bar{\phi}_2 \int_{t_n}^{t_{n+1}} \mathrm{d}t \int_f u_f \, (1 - H) \, \mathrm{d}\boldsymbol{x} \, , \tag{4.10}$$

where the face averages $\bar{\phi}_s$, $s = 1, 2$, are defined as -

$$\bar{\phi}_s = \frac{\int_{t_n}^{t_{n+1}} \mathrm{d}t \int_f \phi \, u_f \, H_s \mathrm{d}\boldsymbol{x}}{\int_{t_n}^{t_{n+1}} \mathrm{d}t \int_f u_f \, H_s \, \mathrm{d}\boldsymbol{x}} \, , \tag{4.11}$$

and $H_1 = H$, $H_2 = 1 - H$. The total flux can be rearranged as a sum of the constituents corresponding to the different 'fluids' -

$$F_f^{(\phi)} = \bar{\phi}_1 \, F_f^{(c)} + \bar{\phi}_2 \, F_f^{(1-c)} \, . \tag{4.12}$$

Expression (4.10) can be written in terms of the fluxes $F_f^{(c)}$ and $F_f^{(1-c)}$, this second one being obtained by replacing H with $1 - H$ in (4.3)

Advection of Density

The density field $\rho(\boldsymbol{x}, t)$ follows the temporal evolution of the generic conserved quantity (4.6) by setting $\phi = \rho$. At the incompressible limit the velocity field is solenoidal (divergence-free), with constant densities in each phase. We can extract the density trivially from the integrals (4.11) to *exactly* obtain $\bar{\rho}_s = \rho_s$. The flux definitions corresponding to ρ becomes -

$$F_f^{(\rho)} = \rho_1 F_f^{(c)} + \rho_2 F_f^{(1-c)} \tag{4.13}$$

Using the above definitions for density fluxes, one can employ any VOF method to construct fluxes of the color function in order to obtain conservative transport for ρ In principle, this should result in the conservation of total mass. However, as we have already pointed out the fact that the CIAM method does not conserve volume exactly [10] , consequently, the advection of the density field (mass) is not consistent with that of the advection of C.

We use the term 'conservative' to express the fact that eq. (4.7) computes the temporal evolution of ρ as a difference of fluxes, instead of velocity times its gradient.

10: This again comes back to the dependence of the compression coefficient on the volume fraction field at the start of each advection substep.

This apparent paradox is resolved by including the compression term on the right hand side of (4.6), in order to ensure consistency. The advection equation for the conserved quantity now becomes -

$$\frac{\partial \phi}{\partial t} + \nabla \cdot (\phi \, \boldsymbol{u}) = \phi \, (\nabla \cdot \boldsymbol{u}) \tag{4.14}$$

This equation can be decomposed into advection substeps corresponding to the direction-split integration framework as follows -

The direction-split integration steps operations for ϕ mirror that of the volume fraction C.

$$\phi^{n,l+1}_{i,j,k} - \phi^{n,l}_{i,j,k} = -F^{(\phi)}_{m-} - F^{(\phi)}_{m+} + \left(\tilde{\phi}^{m}_{1} c^{(1)}_{m} + \tilde{\phi}^{m}_{2} c^{(2)}_{m}\right) \partial^{h}_{m} u_{m} \tag{4.15}$$

The fluxes $F^{(\phi)}_{m\pm}$ follow the definition given in (4.12), , while the cell averages $\tilde{\phi}^{m}_{s}$ are defined as -

$c^{(1)}_{m} = c_m$ is the compression coefficient corresponding to the particular VOF advection method for volume fraction C , while $c^{(2)}_{m} = 1 - c_m$ corresponds to that of the symmetric color fraction $1 - C$.

$$\tilde{\phi}^{m}_{s} = \frac{\int_{t_n}^{t_{n+1}} \mathrm{d}t \int_{\Omega} \phi H_s \partial^{h}_{m} u_m \,\mathrm{d}\boldsymbol{x}}{\int_{t_n}^{t_{n+1}} \mathrm{d}t \int_{\Omega} H_s \partial^{h}_{m} u_m \,\mathrm{d}\boldsymbol{x}} \tag{4.16}$$

Rewriting the direction-split integration operation for ρ we get -

In case of CIAM, the compression coefficient is defined as $c_m = C^{n,l}_{i,j,k}$, whereas in Weymouth-Yue the coefficient is independent of the advection substep l, defined as $c_m = H\left(C^{n}_{i,j,k} - 1/2\right)$, where H is the Heaviside function.

Again, there is no implicit summation rule on m.

$$\rho^{n,l+1}_{i,j,k} - \rho^{n,l}_{i,j,k} = -F^{(\rho)}_{m-} - F^{(\rho)}_{m+} + C^{(\rho)}_{m} \,, \tag{4.17}$$

where the fluxes are given by (4.13) and the compression term is

$$C^{(\rho)}_{m} = \left(\rho_1 c^{(1)}_{m} + \rho_2 c^{(2)}_{m}\right) \partial^{h}_{m} u_m \tag{4.18}$$

For the WY method, the compression terms eventually cancel upon summation over the substeps, therefore resulting in the conservation of mass at the same accuracy as the discrete incompressibility condition $\sum_{m=1}^{3} \partial^{h}_{m} u_m = 0$ is verified [11] .

11: This usually corresponds to the tolerance of the Poisson solver, with a typical value being 10^{-6}.

Advection of Momentum

Within the framework of advection of a generic conserved scalar, we consider momentum advection as transport of the scalar quantities $\phi = \rho u_q$, where $q = 1, 2, 3$ is the component index. Using the definition given in (4.11), we obtain the expression -

The expressions with the 'bar' refer to face weighted averages of the varible in question. Here, $\bar{\phi}_s = \overline{\rho u_q}_s$

$$\overline{\rho u_q}_s = \rho_s \bar{u}_{q,s} \tag{4.19}$$

where $\bar{u}_{q,s}$ is termed as the "advected interpolated velocity", whose precise definition is given as -

$$\bar{u}_{q,s} = \frac{\int_{t_n}^{t_{n+1}} \mathrm{d}t \int_{f} u_q u_f H_s \,\mathrm{d}\boldsymbol{x}}{\int_{t_n}^{t_{n+1}} \mathrm{d}t \int_{f} u_f H_s \,\mathrm{d}\boldsymbol{x}} \tag{4.20}$$

Thus, the direction-spit integration of the momentum can be represented as -

The subscript s denotes the phase or fluid, and f represents the normal components defined on the face centers.

$$(\rho u_q)^{n,l+1}_{i,j,k} - (\rho u_q)^{n,l}_{i,j,k} = -F^{(\rho u)}_{m-} - F^{(\rho u)}_{m+} + \left(\rho_1 \tilde{u}^m_{q,1} c^{(1)}_m + \rho_2 \tilde{u}^m_{q,2} c^{(2)}_m\right) \partial^h_m u_m \tag{4.21}$$

where the momentum fluxes are constructed in the following manner -

$$F^{(\rho u)}_f = \rho_1 \, \bar{u}_{q,1} \, F^{(c)}_f + \rho_2 \, \bar{u}_{q,2} \, F^{(1-c)}_f \,, \tag{4.22}$$

The expression for the "central interpolated velocity" corresponding to the averages $\tilde{\phi}^m_s$ of (4.16) is -

$$\tilde{u}^m_{q,s} = \frac{\int_{t_n}^{t_{n+1}} \mathrm{d}t \int_\Omega u_q \, H_s \, \partial^h_m u_m \, \mathrm{d}\boldsymbol{x}}{\int_{t_n}^{t_{n+1}} \mathrm{d}t \int_\Omega H_s \, \partial^h_m u_m \, \mathrm{d}\boldsymbol{x}} \tag{4.23}$$

Notice that "cloning" the advected velocities $\bar{u}_{q,1}$ and $\bar{u}_{q,2}$ would make it easier to advect a velocity field with a jump on the interface, but would render the overall algorithm quite complicated.

The superscript m is intentionally omitted for the velocities $\tilde{u}^m_q$ in order to avoid cumbersome and complicated notations.

As a reasonable approximation we choose to put $\bar{u}_q = \bar{u}_{q,1} = \bar{u}_{q,2}$ for the "advected interpolated velocity" and $\tilde{u}_q = \tilde{u}_{q,1} = \tilde{u}_{q,2}$ for the "central interpolated velocity". An important simplification which serves as the central model in our development is given by -

Due to the viscous effects and the absence of phase change in our fluid dynamics model, the velocity filed maintains continuity across the interface.

$$F^{(\rho u)}_f = \bar{u}_q F^{(\rho)}_f \tag{4.24}$$

To add clarity to the notion of "central interpolated velocity", one can understand this as the face-centered interpolations of the velocity field (component normal to control surface), which is required to compute the fluxes of volume.

Therefore, the advection substep for the momentum can finally we written as -

$$(\rho u_q)^{n,l+1}_{i,j,k} - (\rho u_q)^{n,l}_{i,j,k} = -\bar{u}_q F^{(\rho)}_{m-} - \bar{u}_q F^{(\rho)}_{m+} + \tilde{u}_q C^{(\rho)}_m \tag{4.25}$$

where the density fluxes are defined in (4.13) and the compression term $C^{(\rho)}$ in (4.18).

Although the weighted averages $\bar{u}_q$ and $\tilde{u}_q$ have been defined, but the manner in which they are estimated shall be covered in the following section.

In the above expression the face-weighted average velocities $\bar{u}_q$ are defined using (4.20) on the corresponding left face $m-$ or right face $m+$.

In the context of the CIAM advection scheme, the compression coefficient for the volume fraction field is $C^{n,l}$, similarly, for the central interpolated velocity we take $\tilde{u}_q = u^{n,l}_q$. Due to the summation of the directional divergences not cancelling out, the resulting momentum transport after three directionally-split advections and the result is not exactly conservative. On the other hand, the compression coefficient is independent of the advection substep in the context of the Weymouth-Yue advection scheme. The final expression for the compression coefficient becomes -

The Weymouth-Yue coefficient is a constant value c, that is independent of direction m.

$$C_m^{(\rho)} = \Big(\rho_1 c + \rho_2(1-c)\Big)\,\partial_m^h u_m\,. \tag{4.26}$$

Since there is no bracketing on the any velocity component, we take $\tilde{u}_q = u_q^n$, which is independent of the substep l. Provided that the velocity field is discretely solenoidal, i.e. $\sum_{m=1}^{3} \partial_m^h u_m = 0$, after the three direction split advections (4.25) one obtains a cancellation of the compression terms, finally resulting in

$$(\rho u_q)_{i,j,k}^{n,3} - (\rho u_q)_{i,j,k}^{n} = -\sum_{\text{faces f}} \bar{u}_q F_f^{(\rho)}. \tag{4.27}$$

The extension of the Weymouth-Yue mass (volume) advection scheme to the consistent transport of momentum allows the discrete transport to be exactly conservative.

Velocity Interpolations

The momentum equation (4.25) can be approximated either 1) in the bulk of the phases or 2) in the neighborhood of the interface. In the first case the expression simplifies considerably since both the density and the color fraction are constant and the spurious compression terms cancel out

$$u_q^{n,3} - u_q^n = -\sum_{\text{faces f}} \bar{u}_q u_f \tag{4.28}$$

We distinguish an "advecting" velocity $u_f = \boldsymbol{u} \cdot \boldsymbol{n}_f$ and an "advected velocity" component $\bar{u}_{q,f}$, involving an average over face f. Both velocity components require an interpolation from their position in the staggered grid to where they are needed. Thus the scheme in the bulk is

$$u_q^{n,3} - u_q^n = -\sum_{\text{faces f}} \bar{u}_q^{(\text{advected})} u_f^{(\text{advecting})} \tag{4.29}$$

while near the interface is

$$(\rho u_q)^{n,3} - (\rho u_q)^n = -\sum_{\text{faces f}} \bar{u}_q^{(\text{advected})} F_f^{(\rho)} + \sum_{m=1}^{3} \tilde{u}_q C_m^{(\rho)} \tag{4.30}$$

Momentum advection in our model is described by these two equations which are solved on a cubic grid with a finite-volume method. In the previous sections we have derived a new expression for the momentum fluxes and the compression term, i.e. the RHS of (4.30), that is consistent with the volume fraction advection.

To estimate the advecting velocities $u_f^{(\text{advecting})}$ we use a centered scheme. The staggered 2D grid of Fig. **??** has the same variables arrangement that is found in 3D on a plane perpendicular to the z-axis and through the pressure point $p_{i,j,k}$. To illustrate the procedure we consider a face perpendicular to the horizontal direction 1, in particular $f = 1-$. There are two cases. In the first case the advected component is not aligned with the face normal, this corresponds to $q = 2$. The u_2 control volume in Fig. **??** is centered on $i, j+1/2, k$, and face $f = 1-$ is then centered on $i-1/2, j+1/2, k$. The advecting velocity $u_{1-}^{(\text{advecting})}$ is not given on this point and has to be interpolated

$$u_{1;i-1/2,j+1/2,k}^{(\text{advecting})} = \frac{1}{2}\left(u_{1;i-1/2,j,k} + u_{1;i-1/2,j+1,k}\right) \tag{4.31}$$

In the second case the advected component is aligned with the face normal, this corresponds to $q = 1$. The u_1 control volume in Fig. **??** is centered on $i+1/2, j, k$ and face $f = 1-$ is then centered on i, j, k. The interpolation is now

$$u_{1;i,j,k}^{(\text{advecting})} = \frac{1}{2}\left(u_{1;i-1/2,j,k} + u_{1;i+1/2,j,k}\right) \tag{4.32}$$

Now we turn to the interpolation of the *advected* velocity $\bar{u}_q$ in (4.30). The interpolants we use in this case are one-dimensional and operate on the velocities u_q, on the center of their control volume, that are regularly spaced on a segment aligned with the direction of the advection, that is perpendicular to face f. We still consider an advection along the horizontal direction 1. In Fig. 4.1, with the lighter notation $\phi = u_q$, we need to interpolate the advected velocity on the left face of the reference control volume Ω. For the advected velocity u_1 and the advecting velocity (4.32) on face $f = 1-$ the correspondence with the ϕ values in Fig. 4.1 is

$$\phi_{-3/2} = u_{1;i-3/2,j,k}, \quad \phi_{-1/2} = u_{1;i-1/2,j,k}, \quad \phi_{1/2} = u_{1;i+1/2,j,k}, \quad \cdots \tag{4.33}$$

while for the advected velocity u_2 and the advecting velocity (4.31) is

$$\phi_{-3/2} = u_{2;i-2,j+1/2,k}, \quad \phi_{-1/2} = u_{2;i-1,j+1/2,k}, \quad \phi_{1/2} = u_{2;i,j+1/2,k}, \quad \cdots \tag{4.34}$$

The extension of these results to an advection along the other two directions $q = 2, 3$ follows easily. We need to predict ϕ_0 on face $f = 1-$ in Fig. 4.1 to serve as an approximation of $\bar{u}_q$ given in (4.20). We consider an interpolation function f that computes this value as a function of the four nearest points, and in an upwind manner based on the sign of the *advecting* velocity u_f

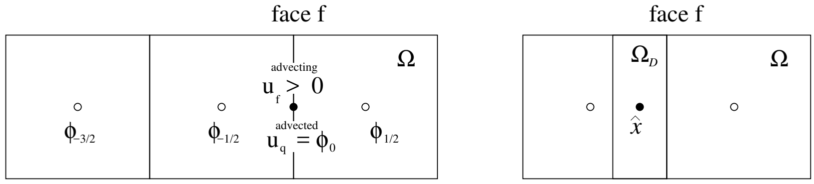

(a) (b)

Figure 4.1: The reference control volume Ω for the advected velocity component $\phi = u_q$ is shown. A horizontal advection is here considered and both the advecting velocity u_f and the advected velocity require an interpolation for their value on the left face $f = 1-$: (a) the value $\bar{u}_q = \phi_0$ (full circle) is interpolated (see **??**) from the values $\phi = u_q$ on the nodes (open circles); (b) a more sophisticated interpolation predicts the value $\phi(\hat{x})$ where $\hat{x}$ is at the center of the "donating" region Ω_D (see **??**).

$$\phi_0 = f\left(\phi_{-3/2}, \phi_{-1/2}, \phi_{1/2}, \phi_{3/2}, \operatorname{sign}(u_f)\right) \tag{4.35}$$

In this study we have extensively tested two kinds of interpolations:

1. a scheme that uses a QUICK third order interpolant in the bulk, away from the interface and a simple first order upwind flux near the interface. We call this scheme QUICK-UW;
2. a scheme that uses a Superbee slope limiter [**roe1985some**] for the flux in the bulk and a more complex Superbee limiter tuned to a shifted interpolation point near the interface. We naturally call this scheme "Superbee".

The details of the two schemes are given in **??**.

4.3 Advection on Staggered Grids

Shifted Fractions Method

Sub-Grid Method

Source Terms

Numerical Benchmarks | 5

In the upcoming sections, we demonstrate the robustness and accuracy of our class of mass-momentum consistent numerical methods when applied to challenging high density-ratio flow configurations, primarily in comparison to the version of our method which does not maintain consistency between the mass and momentum advection. Most of the standard tests that exist in the current literature concerning numerical methods to tackle liquid-gas flows such as the decay of spurious currents in static and moving droplets, viscous damping of capillary waves etc., are carried out in the absence of any density jump (or viscosity jump) across the interface separating the fluids. In this chapter, we shall take a closer look in detail at the behavior of our methods when dealing with difficulties that arise due to the non-linear coupling between interfacial deformation/propagation, capillary and viscous forces, especially in the regime where the material properties across the interface are separated by orders of magnitude, particularly in which the flow features in question are poorly resolved.

In order to assess the performance of the different methods, we shall use an easier nomenclature to describe the different methods, which are as follows :

- **M1** Method with non-consistent momentum-mass transport.
- **M2** Method with consistent momentum-mass transport, but not conservative. Uses half-fractions strategy.
- **M3** Method with consistent and conservative momentum-mass transport. Uses sub-grid strategy.

5.1 Static Droplet

A popular numerical benchmark in the existing literature relevant to surface tension dominated flows is the case of a spherical droplet of the denser fluid immersed in a quiescent surrounding medium of the lighter fluid. In the hydrostatic limit of the Navier-Stokes equations, the droplet should stay in equilibrium, with a curvature induced pressure jump across the interface corresponding to Laplace's equilibrium. In practice however, numerically reproducing such a trivial equilibrium condition is not as straighforward, as there exists a slight difference between the initial numerical interface and the exact analytical shape of the sphere, thereby resulting in the generation of the well documented '*spurious*' or '*parasitic*' currents of varying intensity in the velocity field [37–39] . A lot or progress has been made since in the context of *well-balanced* surface tension formulations, that ensure consistency between the numerical stencils used for the discretization of the pressure gradient and the Heaviside approximation ($n\delta_s$) that projects the the surface force distribution onto the control volumes [20, 40]. A significant contribution to the interpretation of these parasitic currents within the well-balanced

[37]: Lafaurie et al. (1994), 'Modelling merging and fragmentation in multiphase flows with SURFER'
[38]: Harvie et al. (2006), 'An analysis of parasitic current generation in volume of fluid simulations'
[39]: Popinet et al. (1999), 'A front-tracking algorithm for accurate representation of surface tension'

framework was made by Popinet [20] which demonstrated that given sufficient time (of the order of viscous dissipation time-scales), a well-balanced method will relax to the '*numerical*' equilibrium shape through the damping of the 'physically consistent' numerical capillary waves, therefore allowing us to recover the exact (to machine precision) Laplace equilibrium condition.

Setup

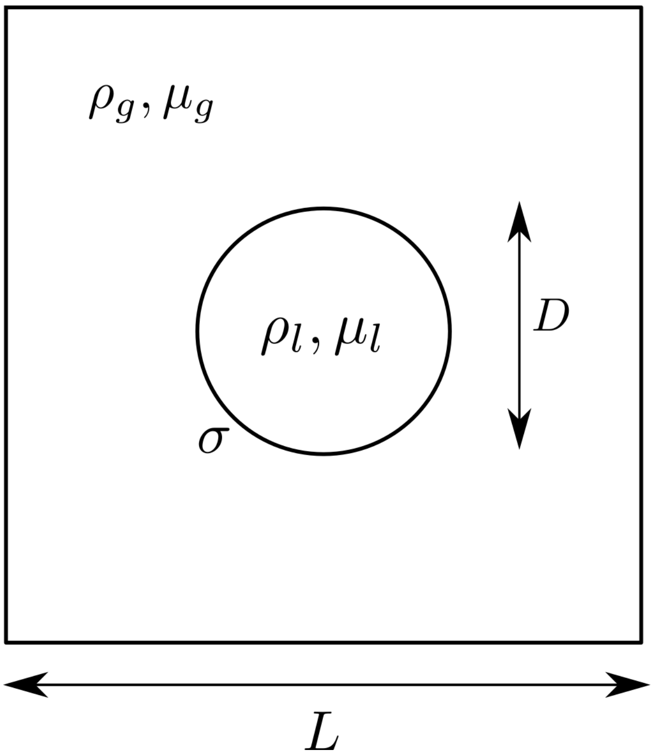

Figure 5.1: Schematic of the static droplet of dense fluid surrounded by a quiescent medium of lighter fluid. A 40×40 grid is employed to spatially discretize the domain.

The key difference in our implementation of this classic test case from that of Popinet [20] is that we consider the effect of density contrast across the interface separating the fluids. As we have previously discussed, a sharp density jump across the interface may have an amplification effect on the numerical errors incurred as a result of interfacial reconstructions, curvature estimation and various other truncations, thereby rendering the method unstable. We demonstrate that in our framework of mass consistent momentum transport coupled with a well-balanced surface tension discretization, density-ratios as large as 1000 : 1 can be simulated without loss of numerical stability, in conjuction with the ability to recover the exact numerical equilibrium through the dissipation of spurious currents within relevant time-scales [1] .

[20]: Popinet (2009), 'An accurate ac solver for surface-tension-driven i cial flows'

1: The viscous time-scale corresponding to the droplet length-scale is the most commonly used in literature.

We consider a circular droplet of size D placed at the centre of a square domain of side L. The densities of the heavier and lighter phases are ρ_l and ρ_g respectively, likewise for the viscosities μ_l and μ_g, and σ being the surface tension coefficient (fig. 5.1). The ratio of the droplet size to the box is chosen as $D/L = 0.4$, coupled with a numerical resolution of $D/\Delta x = 16$ (where Δx is the grid size). As for boundary conditions, we use symmetry conditions on all sides of the square domain.

The problem incorporates two natural time-scales, the capillary oscillation scale and the viscous dissipation scale, which are defined below :

$$T_\sigma = \left(\frac{\rho_l D^3}{\sigma}\right)^{1/2} \quad , \quad T_\mu = \frac{\rho_l D^2}{\mu_l} \tag{5.1}$$

The ratio of these time-scales give us -

$$\frac{T_\mu}{T_\sigma} = \sqrt{\rho_l \sigma D}/\mu_l = \sqrt{La} \tag{5.2}$$

where La is the Laplace number based upon the heavier fluid. In the present study, we introduce the density-ratio ρ_l/ρ_g as another important parameter. In order to rescale our 'parasitic' velocity field, we define a velocity scale based on capillary oscillations as -

$$U_\sigma = \sqrt{\sigma/\rho_l D} \tag{5.3}$$

Additionally, the time-step in our numerical simulation must be smaller than the oscillation period corresponding to the grid wavenumber (fastest capillary wave with a time period $\sim \left(\rho_l \Delta x^3/\sigma\right)^{1/2}$) as a stability criterion [2] , as our surface tension model is explicit in time. For the scope of the present study, we shall not consider any viscosity contrast between the two fluids while varying the density-ratio, therefore $\mu_l/\mu_g = 1$ for all the cases under study.

2: Similar criteria are defined on the basis of the viscous and advection operators as well, with the smallest amongst the three selecting the numerical time-step

Decay of Spurious Currents

In figures 5.2 to 5.4, we illustrate the decay of the root-mean-square of the spurious currents as a function of time, in the case of four different density-ratios, with three different Laplace numbers for each ratio. The first figure (5.2) refers to simulations carried out without consistency between the momentum-mass transport (**M1**), the second (5.3) corresponds to that of the consistent but not conservative method (**M2**), and final one (5.4) refers to that of the consistent and conservative method (**M3**). The time is rescaled by the viscous dissipation scale, and the spurious currents by the capillary velocity scale. We have two main observations, the rapid decay of the rescaled spurious currents for all combinations of density-ratios and Laplace numbers within approximately $0.2T_\mu$, and the slower re-growth of the currents in question for combinations of non-unity density-ratios and large Laplace numbers, in all simulations except those carried out with **M3**. With method **M3**, the decayed currents keep hovering around levels of machine precision for remainder of time. Although there is a re-growth of the currents using the consistent method (**M2**) after $0.2T_\mu$, the behavior is not quite alarming as the rate of this re-growth is quite low. Therefore, out of all the methods tested, the consistent and conservative method (**M3**) does seem to demonstrate the desired performance, especially when it comes to combinations of large density contrasts coupled with large Laplace numbers.

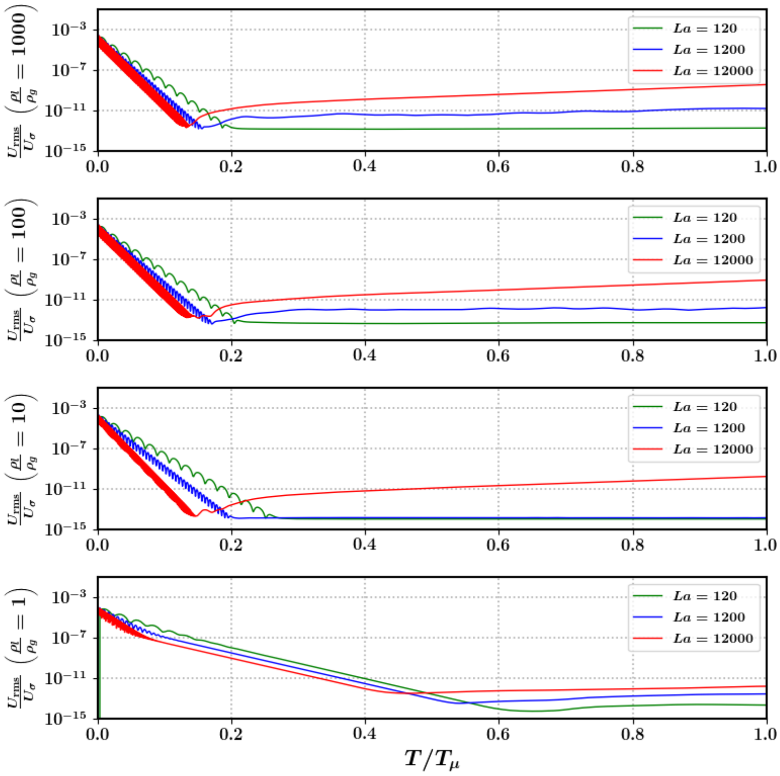

Figure 5.2: M1 Decay of normalized spurious currents as a function of viscous dissipation time-scales for different density-ratios and Laplace numbers. The currents seem to initially decay quickly for all higher density-ratios, and relax to the numerical equilibrium curvature even within $0.2 \cdot T_\mu$. For combinations of large ρ_l/ρ_g and large La, the spurious currents seem to grow back to an order of magnitude (10^{-8}) which is quite far from that of machine precision (10^{-14}).

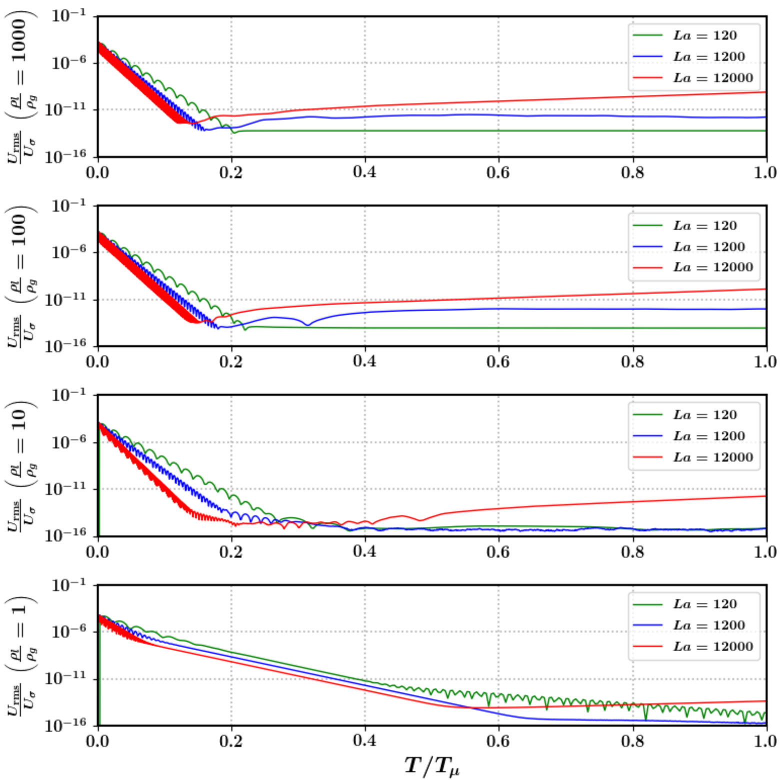

Figure 5.3: M2 Decay of normalized spurious currents as a function of viscous dissipation time-scales for different density-ratios and Laplace numbers. The currents seem to initially decay quickly for all higher density-ratios, and relax to the numerical equilibrium curvature even within $0.2 \cdot T_\mu$. For combinations of large ρ_l/ρ_g and large La, the spurious currents seem to grow back to an order of magnitude (10^{-8}) which is quite far from that of machine precision (10^{-14}). No considerable improvement is observed with respect to **M1**.

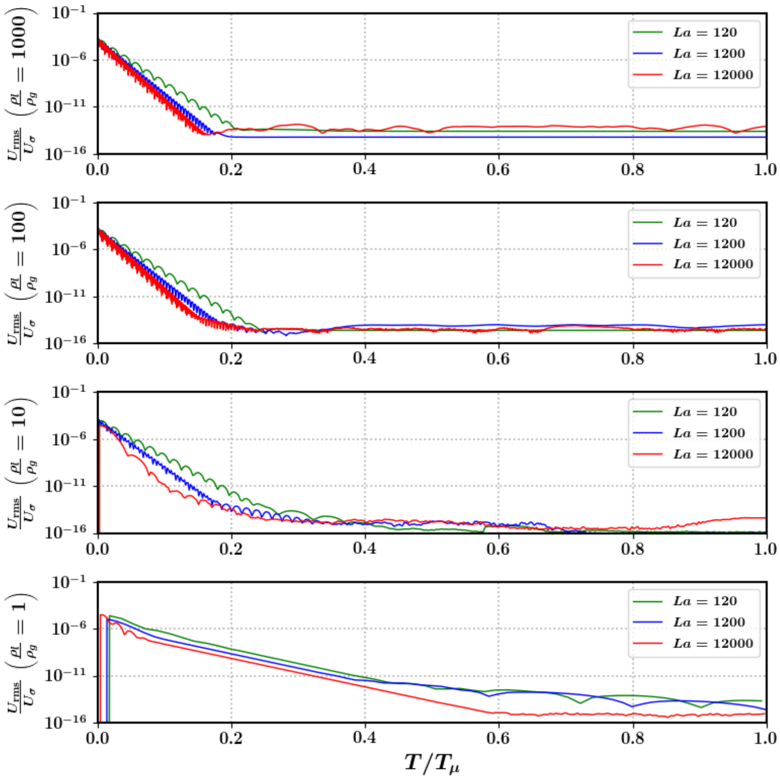

Figure 5.4: M3 Decay of normalized spurious currents as a function of viscous dissipation time-scales for different density-ratios and Laplace numbers. The currents seem to decay very quickly in the case of higher density-ratios, and relax to the numerical equilibrium curvature even within $0.2 \cdot T_\mu$. For all combinations of ρ_l/ρ_g and La numbers, the decayed spurious currents are not observed to grow back as in the cases of **M1** and **M2**, and hover around values close to machine precision (10^{-14}).

Spatial Convergence

Once the solution relaxes to a numerical equilibrium curvature (spurious currents are approximately at the order of machine precision), there still exists a difference between the numerical curvature and the exact analytical curvature corresponding to the spherical (circular) shape. We use the definitions of the shape errors as introduced in the seminal work of Popinet [20] to assess the convergence of our class of methods to the exact (analytical) curvature as we increase spatial resolution. The norms are defined as follows :

$$L_2 = \sqrt{\frac{\sum_i \left(C_i - C_i^{\mathrm{exact}}\right)^2}{\sum_i}} \quad , \quad L_\infty = \max_i \left(|C_i - C_i^{\mathrm{exact}}|\right) \tag{5.4}$$

where C_i is the volume fraction of a cell after the solution has relaxed to the numerical equilibrium curvature, and C_i^{exact} is the volume fraction corresponding to the exact circular shape which was initialized at the start of the simulation.

Fig. 5.5 demonstrates the behavior of the shape errors defined in eqn. 5.4 for the case of the most stringent parameter combination ($\rho_l/\rho_g = 1000$, $La = 12000$) as a function of the droplet resolution. As one can clearly observe, all the methods tested display a roughly second-order convergence in space for both the error norms. In terms of the L_2 norm, the consistent and conservative method (**M3**) does indeed achieve smaller errors as compared to both **M1** and **M2** for all spatial resolutions. As a minor remark, there is not much to discern in terms of shape error when it comes to comparing the performances of the consistent (**M2**) method with the non-consistent one (**M1**).

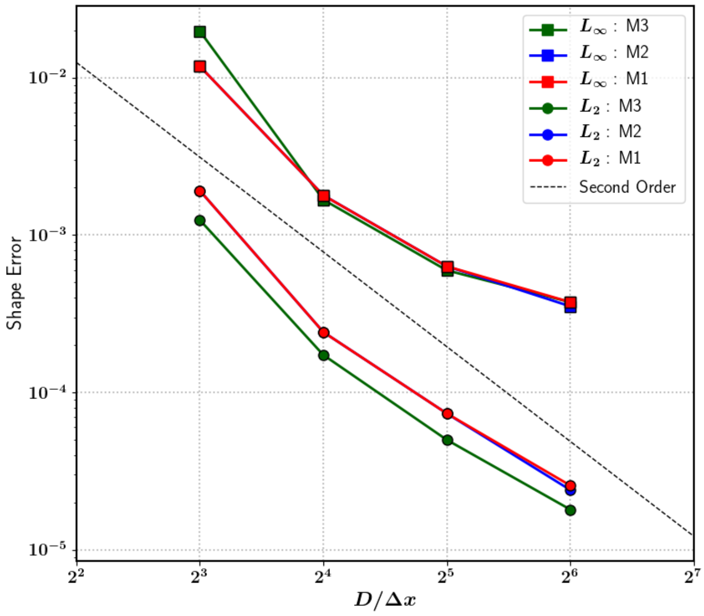

Figure 5.5: Second-order spatial convergence for the spurious current error norms corresponding to the most stringent parameter combination (ρ_l/ρ_g = 1000 , La = 12000) . Both of the norms (L_∞ and L_2) seem to demonstrate a roughly second order rate of spatial convergence with each of the methods tested. However, **M3** has a marginally lower L_2 error compared to both **M1** and **M2** for all resolutions tested. There is negligible difference observed in the shape errors between **M1** and **M2** in both of the norm definitions.

5.2 Moving Droplet

An incisive numerical setup that enables us to evaluate the accuracy of the coupling between interfacial propagation and surface tension discretization was first proposed by Popinet [20], and subsequently employed in the comparative study of Abadie et al. [41] . The manner in which this test differs from that of the static droplet is the addition of a uniform background velocity field, therefore serving as a better representation of droplets in complex surface tension dominated flows where they might be advected by the mean flow. In terms of the Laplace equilibrium, the hydrostatic solution is still valid in the frame of reference of the moving droplet. The point at which the solution in the moving reference frame diverges from that of the static droplet (5.1) is through the continuous injection of noise at the scale of the grid size. This 'numerical' noise emanates from the perturbations to the curvature estimates, which are in turn induced by the interfacial reconstructions carried out to propagate the interface (temporal integration) . These fluctuating errors act as source terms for the momentum, thereby transforming the problem into that of viscous dissipation in the presence of continuous forcing (in the reference frame of the moving drop).

Setup

In the present study, we evaluate our class of methods using the advection of a droplet in a spatially periodic domain using an identical setup as [20], but with the important difference of including sharp density jumps across the interface as well as using lower spatial resolutions.

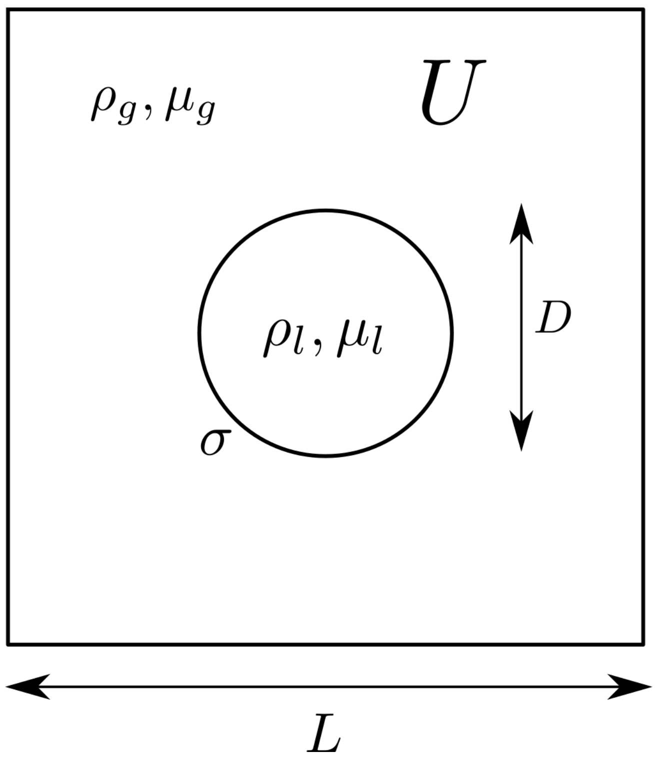

Figure 5.6: Schematic of the droplet of dense fluid advected in a surrounding medium of lighter fluid. A 50×50 grid is employed to spatially discretize the domain, which is spatially periodic in the direction of droplet advection.

As previously discussed (5.1), high density-ratios tend to amplify the fluctuations induced by the myriad numerical approximations (interface reconstruction, curvature estimation etc) involved in the algorithm.

We consider a circular droplet of diameter D placed at the centre of a square domain of side L. The densities of the heavier and lighter phases are ρ_l and ρ_g respectively, likewise for the viscosities μ_l and μ_g, and σ being the surface tension coefficient (fig. 5.6). A uniform velocity field $\boldsymbol{U}$ is initialized on the entire domain (only a horizontal component). The ratio of the droplet size to the box is $D/L = 0.4$, with $D/\Delta x = 20$ (Δx being the grid size. [3]). As for boundary conditions, we use symmetry conditions on the top and bottom sides, and periodic boundary conditions on the horizontal direction (along which advection by U takes place). We characterize by problem by introducing the following adimensional parameters (based on the heavier fluid) :

3: In Popinet [20], a resolution of $D/\Delta x = 25.6$ corresponding to a grid of 64×64 is used

$$La = \frac{\rho_l \sigma D}{\mu_l^2} \quad , \quad We = \frac{\rho_l U^2 D}{\sigma} \tag{5.5}$$

In addition to the capillary and viscous time-scales for the static case (eqns. 5.1), we have an additional scale defined as :

$$T_u = D/U \tag{5.6}$$

which is the time-scale of advection. In our subsequent analysis, we shall use T_u and U as the time and velocity scales, repectively.

Evolution of Spurious Currents

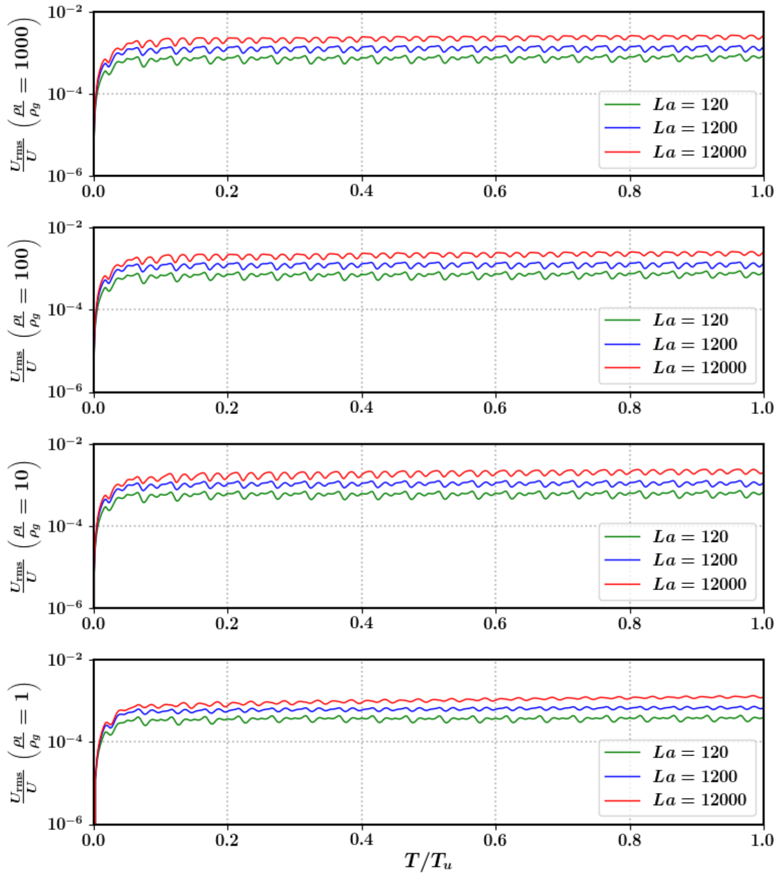

Figure 5.7: M1 Time evolution of normalized spurious currents as a function of advection time-scales (T_u) for different combinations of density-ratio and Laplace numbers. The currents seem to hover around 10^{-3}, with a larger Laplace number corresponding to a higher error for all density-ratios. $We = 0.4$ for all the cases presented.

Figures 5.7 to 5.9 depict the evolution of the root-mean-square (RMS) error of the velocity field in the moving frame of reference, as a function of different Laplace numbers, spanning over density-ratios separated by orders of magnitude. The first figure (5.7) refers to simulations carried out without consistency between the momentum-mass transport (**M1**), the second (5.8) corresponds to that of the consistent but not conservative method (**M2**), and final one (5.9) refers to that of the consistent and conservative method (**M3**). We again have a couple of important observations, the first being that spurious currents do not decay to machine precision as in static droplet case for all of the combinations and methods tested, instead they oscillate around a mean value of the order of $0.1 - 0.01\%$ of the constant field U. The second observation is regarding the significantly smaller error (almost by one order of magnitude) in the case of the consistent and conservative method (**M3**) when compared to that of **M1** and **M2**. As a minor remark, in case of large Laplace numbers, the **M3** method displays a slight upward trend in the error evolution, which is not the case in either **M1** or **M2**. This is not too worrisome as the growth is over a time-scale much larger than T_u, with the oscillations corresponding to a time-scale of the order $U/\Delta x$. All of the plots in figures 5.7 to 5.9 correspond to $We = 0.4$, alongside an additional simplification of equal viscosities across the interface i.e $\mu_l/\mu_g = 1$.

As evindenced by the persistence of these spurious currents due to the

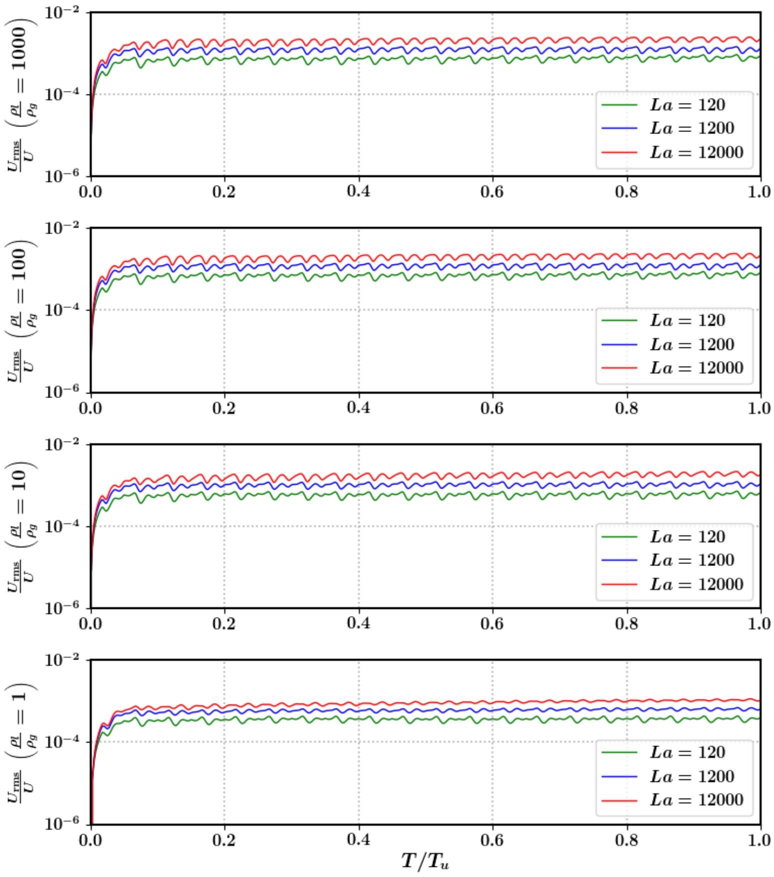

Figure 5.8: M2 Time evolution of normalized spurious currents as a function of advection time-scales (T_u) for different combinations of density-ratio and Laplace numbers. There seems to be no appreciable difference from the evolution seen in the case of **M1** (fig. 5.7). The currents seem to hover around 10^{-3}, with a larger Laplace number corresponding to a higher error for all density-ratios. $We = 0.4$ for all the cases presented.

addition of grid-level noise emanating from interfacial reconstructions, further advancements should be made with respect to the combined performace of the interfacial transport, curvature computation and the surface tension model. Nonetheless, all the methods tested do seem to be quite numerically stable when dealing with the high density-ratios, and are not subject to rapid uncontrollable amplifications of the interfacial perturbations even for high Laplace numbers.

Spatial Convergence

In order to evaluate the performance of our class of methods at different resolutions, we define the errors as the maximum values of the norms L_∞ and L_2 of the rescaled field U_{rms}/U over time (5 times T_u). In fig. 5.10, we show the scaling of the error as a function of spatial resolution for the most stringent case of $\rho_l/\rho_g = 1000$, $La = 12000$, for each of our different methods. As similarly observed in section 5.1, in terms of both L_∞ and L_2 norms, there is no appreciable difference in the behaviors of **M1** and **M2**. For **M3**, we do observe significantly lower maximum errors compared to other two methods, but at a cost of slightly less than first-order convergence. The overall convergence behavior of the class of methods we have tested seem to be consistent with earlier studies of Popinet [20] and others [4] .

4: In existing literature, convergence rates have only been studied in case of equal density fluids across the interface

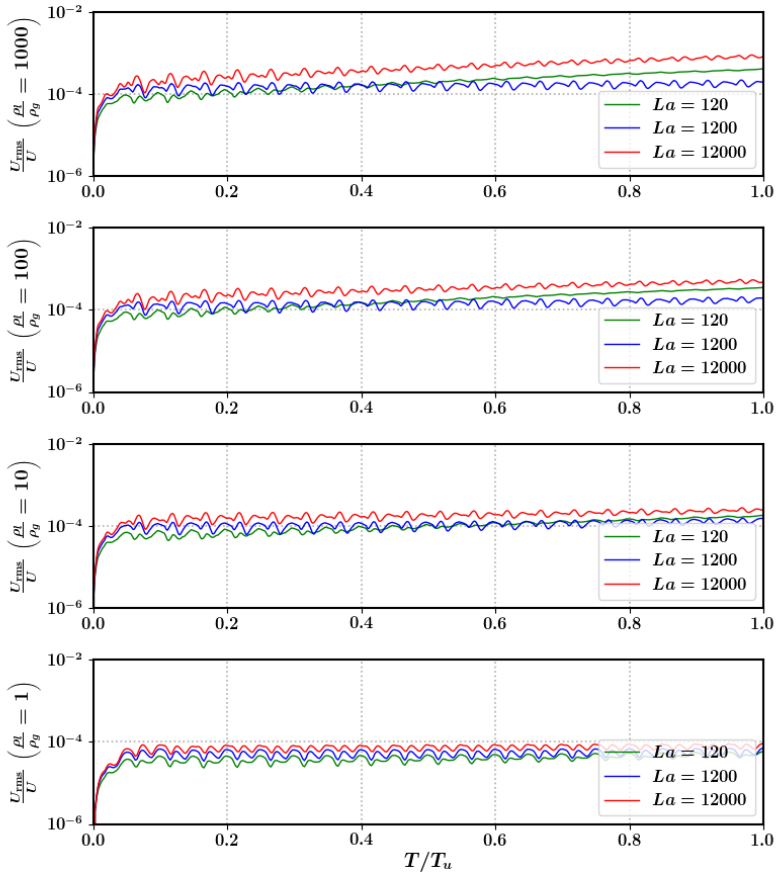

Figure 5.9: M3 Time evolution of normalized spurious currents as a function of advection time-scales (T_u) for different combinations of density-ratio and Laplace numbers. In terms of the errors observed in **M1** and **M2**, we observe a decrease of roughly one order of magnitude. Although an upward trend is observed for large Laplace numbers, the growth rate is quite low. The currents seem to hover slightly above 10^{-4}, with larger Laplace numbers corresponding to larger errors for all density-ratios. $We = 0.4$ for all the cases presented.

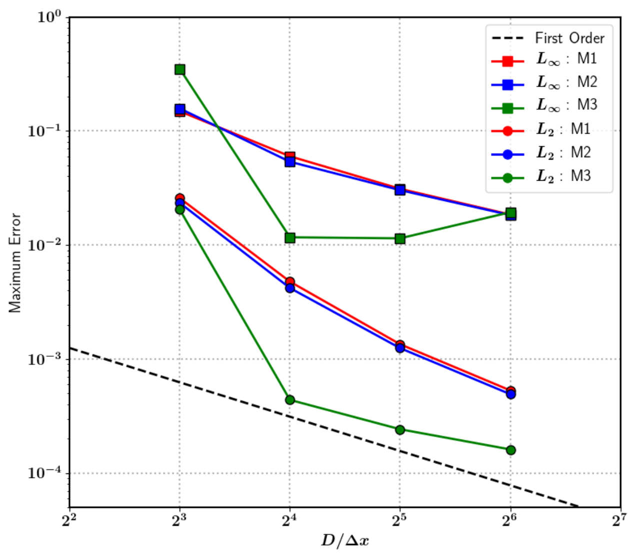

Figure 5.10: First-order (approximately) spatial convergence of the maximum of the spurious current error norms in the frame of reference of the moving droplet, for the most stringent parameter combination ($\rho_l/\rho_g = 1000$, $La = 12000$, $We = 0.4$). Methods **M1** and **M2** display similar convergence properties, whereas **M3** leads to significantly lower errors even though it doesn't quite follow the first-order convergence rate.

Error Dependence : Laplace & Weber numbers

As the final point of inquiry into the performance of our class of methods, figures 5.11 and 5.12 demonstrate the influence of the Laplace and Weber numbers on the behavior of the maximum error norm, carried out for the largest density-ratio ($\rho_l/\rho_g = 1000$). We only present the results obtained using the consistent and conservative method (**M3**), for a resolution corresponding to $D/\Delta x = 25.6$. As we can observe, the error (both L_∞

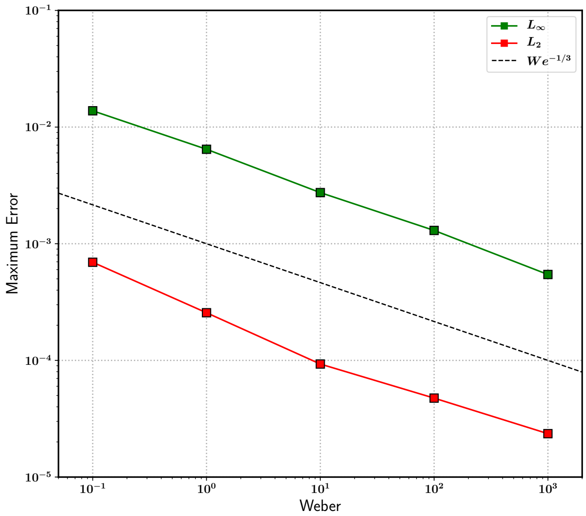

Figure 5.11: Scaling of the maximum error norm as a function of Weber (La = 12000, ρ_l/ρ_g = 1000).

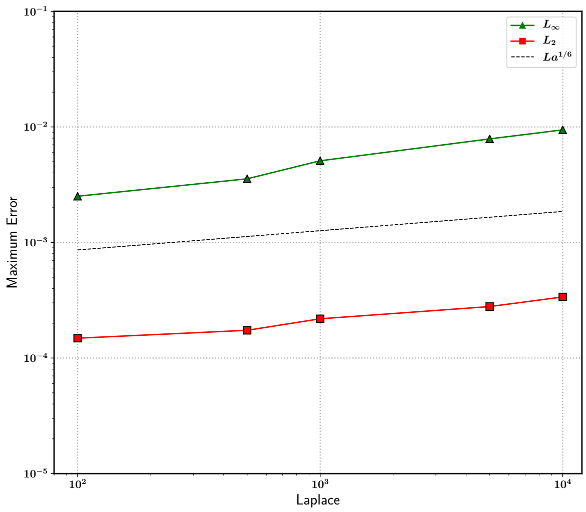

Figure 5.12: Scaling of the maximum error norm as a function of Laplace (We = 0.4, ρ_l/ρ_g = 1000).

and L_2) scales as $We^{-1/3}$ over 4 orders of magnitude, which is different from the $We^{-1/2}$ scaling observed by Popinet [20] [5] . In terms of Laplace numbers, the errors scale as $La^{1/6}$ over two orders of magnitude, which is the same as that observed in [20] (for equal densities).

5: Although Popinet [20] had equal densities (ρ_l/ρ_g = 1)

5.3 Capillary Wave

One of fundamental features of immiscible multiphase flows involving interfaces are the presense and propagation of capillary waves. Therefore, a robust and accurate numerical method should not only be able to adequately resolve, but also accurately emulate the spatio-temporal evolution of such surface tension induced oscillations. A brief outline on the state-of-the-art numerical implementations of capillary waves (and surface tension models in general) existing in current literature is provided by Popinet in the comprehensive review [6] .

[6]: P
surfa

Setup

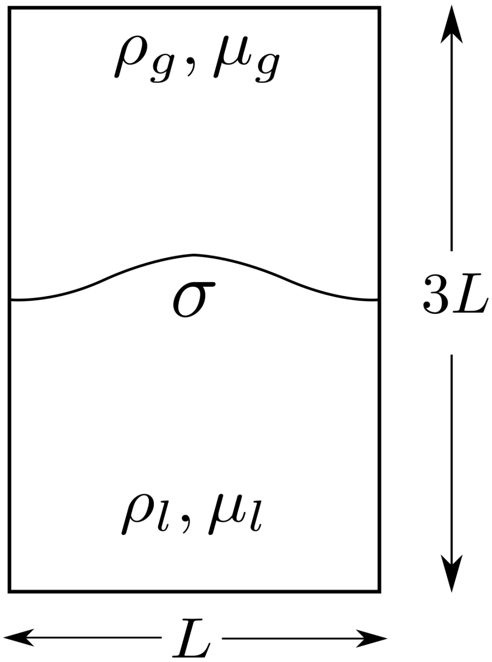

Figure 5.13: Schematic of the initially perturbed planar interface separating two immiscible fluids of different densities and viscosities. A spatial resolution of 32×96 is used for spatial discretization (compared to 64×192 in Popinet [20]), with the width of the box corresponding to the size of the perturbed wavelength.

In the present study, we evaluate the accuracy of our class of methods by comparing with an analytical solution of damped capillary oscillations. Generally, analytical solutions exist only for cases corresponding to extremely small initial perturbations, that too either in the inviscid limit (Lamb [42]) or the asymptotic limit of vanishing viscosity (Prosperetti [43, 44]). For our purposes, we use the configuration of the viscosity-damped capillary oscillations of a planar interface, as was first implemented and popularized by Popinet & Zaleski [39].

[42]: Lamb (1993), *Hydrodynamics*
[43]: Prosperetti (1980), 'Free oscillations of drops and bubbles: the initial-value problem'
[44]: Prosperetti (1981), 'Motion of two superposed viscous fluids'

We consider a rectangular domain of dimensions $L \times 3L$, where L corresponds to the wavelength of our initial perturbation. The densities of the heavier and lighter phases are ρ_l and ρ_g respectively, likewise for the viscosities μ_l and μ_g, and σ being the surface tension coefficient (fig. 5.13). An intial perturbation amplitude of $L/100$ is used, coupled with a numerical resolution given by $L/\Delta x = 32$ (Δx being the grid size). Symmetry conditions are applied on the top and bottom sides, with periodic conditions along the horizontal direction. We use the following adimensional parameters to characterize our problem :

$$T_0 = T\omega_0 \quad , \quad La = \frac{\rho_l \sigma L}{\mu_l^2} \tag{5.7}$$

where La is the Laplace number based on the heavier fluid, and ω_0 is defined using the dispersion relation used in Popinet [20] given as :

$$\omega_0^2 = \frac{\sigma k^3}{2\rho_l} \quad , \qquad \text{where} \quad k = \frac{2\pi}{L} \tag{5.8}$$

The dispersion relation is obtained via linear stability analysis at the inviscid limit [42] . In order to evaluate the influence of density-ratio on the performance of our class of methods, we use three different numerical setups keeping the same Laplace number ($La = 3000$) as follows :

[42]: Lamb (1993), *Hydrodynamics*

- $\rho_l/\rho_g = 1$, $\mu_l/\mu_g = 1$ (Popinet [20])
- $\rho_l/\rho_g = 10$, $\mu_l/\mu_g = 1$
- $\rho_l/\rho_g = 1000.0/1.2$, $\mu_l/\mu_g = 1.003 \cdot 10^{-3}/1.8 \cdot 10^{-5}$ (Air-Water)

The final setup corresponds to that of an air-water interface (physical properties corresponding to 20^o Celsuis), which is the most stringent due to the significant density and viscosity jumps.

Comparison with Prosperetti Solution

The theoretical solution to this configuration corresponds to the closed-form expressions of the planar interface shape evolution established by Prosperetti [43, 44], which takes into account the finite time-scales at which the vorticity (generated due to interface oscillations) diffuses into the bulk medium. These closed-form expressions are subsequently integrated using a fourth-order Runge-Kutta time integrator (details of which not described here), and used to assess the accuracy of the results obtained by our class of numerical methods.

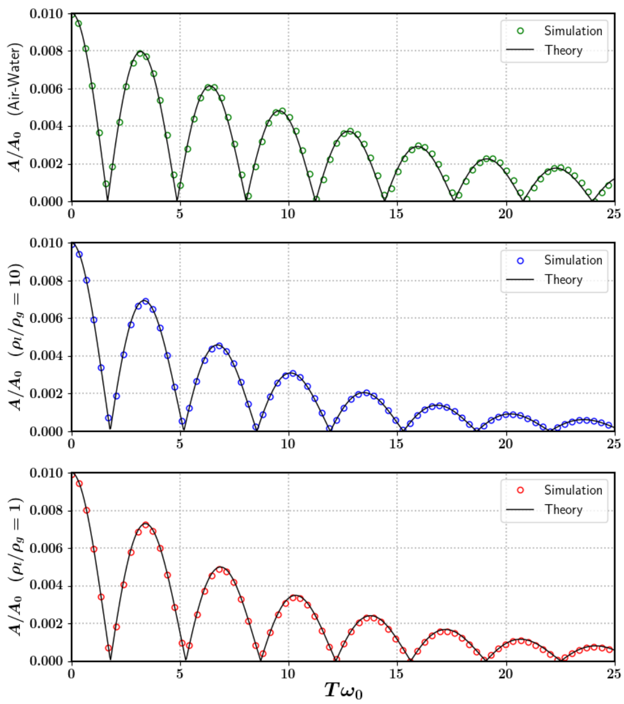

Figure 5.14: M1 Time evolution of the amplitude of the planar interface undergoing damped capillary oscillations, comparing the solution obtained by our numerical method with the closed-from Prosperetti solution. More or less good agreement with theory is observed for all the density-ratios tested.

As we can in figures 5.14 to 5.16, solutions from our class of numerical methods (circles) are compared to that of the theoretical (Prosperetti) solution (black curves), where the amplitude is normalized by the initial value (A_0) and the time rescaled by T_0. The first figure (5.14) refers to simulations carried out by the non-consistent method, the second (5.15) corresponds to that of the consistent method, and the final one (5.16) refers to that of the consistent and conservative method. We observe that there is hardly any appreciable qualitative difference between the results obtained via the different methods **M1**, **M2** and **M3**, although **M3** does seem to perforn marginally better when it comes to the most stringent case (air-water configuration). Surprisingly, even the non-consistent method (**M1**) does not seem to show any un-physical interfacial deformations for all the density-ratios tested, and that it is difficult to distinguish between the different methods for the lower density-ratios.

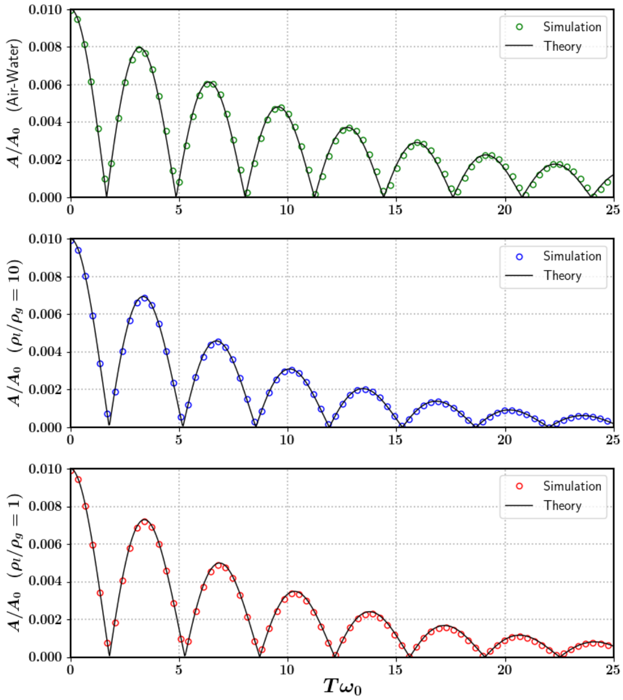

Figure 5.15: M2 Time evolution of the amplitude of the planar interface undergoing damped capillary oscillations, comparing the solution obtained by our numerical method with the closed-from Prosperetti solution. Behavior is quite similar to **M1**, with good agreement with theory for all the density-ratios tested.

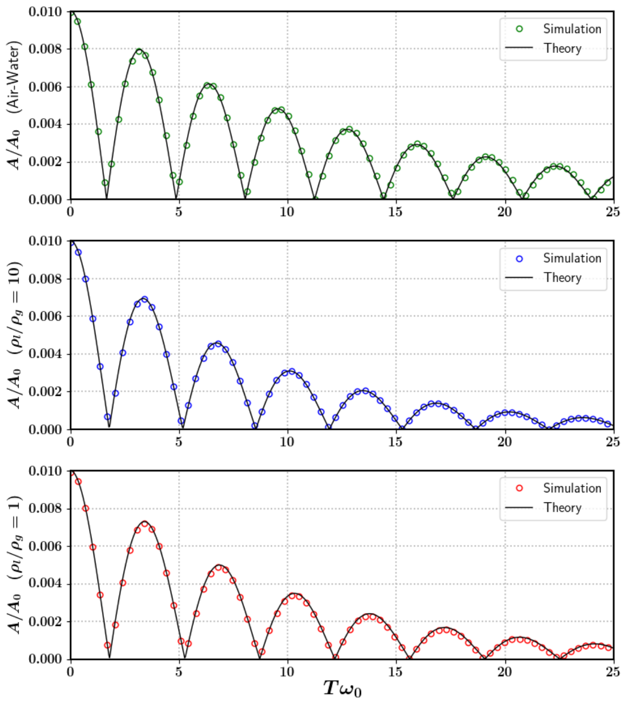

Figure 5.16: M3 Time evolution of the amplitude of the planar interface undergoing damped capillary oscillations, comparing the solution obtained by our numerical method with the closed-from Prosperetti solution. Slightly better agreement with theory when comparing to **M1** and **M2**, for all density-ratios tested.

Spatial Convergence

The next step in our evaluation would be to quantify the accuracy of our numerical results to the Prosperetti solution using an integral (in time) error norm, the same as defined in [20] :

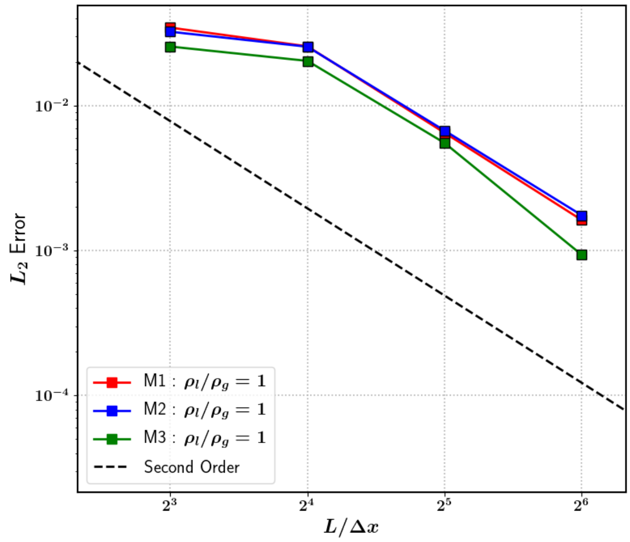

Figure 5.17: Comparison of spatial convergence for the case of $\rho_l/\rho_g = 1, La = 3000$, for our class of methods. There is no viscosity jump across the interface. All methods seem to demonstrate approximately second-order convergence. There seems to be no appreciable difference in the behavior of **M1** and **M2**, with **M3** displaying marginally lower errors compared to the others.

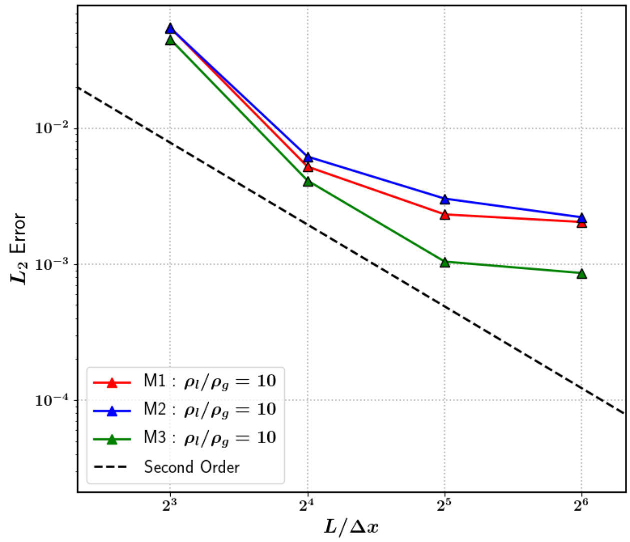

Figure 5.18: Comparison of spatial convergence for the case of $\rho_l/\rho_g = 10, La = 3000$, for our class of methods. Again, there is no viscosity jump across the interface. All methods seem to demonstrate approximately second-order convergence upto $/\Delta x = 32$, beyond which there is a slight saturation in the rate of convergence. Qualitatively, **M1** and **M2** demonstrate similar behavior, with **M3** delivering slightly lower errors. In case of **M3**, the errors are marginally lower compared to **M1** and **M2** for higher resolutions.

$$L_2 = \frac{1}{L}\sqrt{\frac{\omega_0}{25}\int_{t=0}^{T}(h - h_{exact})^2} \tag{5.9}$$

where h is the maximum inteface height obtained using our numerical simulations, and h_{exact} being the maximum height obtained via time integration of the Prosperetti solution. In figures 5.17 to 5.19 we demonstrate the rate of spatial convergence of the L_2 error norms for different density-ratios, simultaneously comparing the behavior of the different methods **M1**, **M2** and **M3** at each density-ratio. In all the results presented, we maintain $La = 3000$ for all density-ratios, spatial resolutions

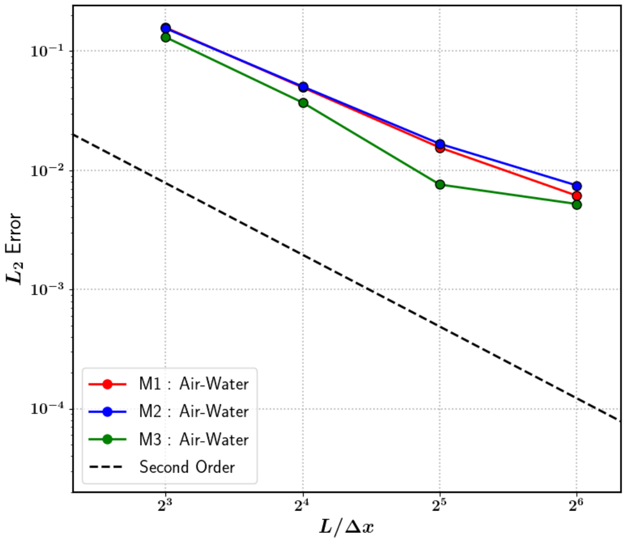

Figure 5.19: Comparison of spatial convergence for the Air-Water case corresponding to $\rho_l/\rho_g = 1000.0/1.2$, $\mu_l/\mu_g = 1.003 \cdot 10^{-3}/1.8 \cdot 10^{-5}$, $La = 3000$, for our class of methods. All methods seem to demonstrate approximately second-order convergence. No appreciable difference is observed between **M1** and **M2**, with **M3** delivering slightly lower errors although there is some saturation in the convergence rate at higher resolutions.

and methods tested.

In figure 5.17 we observe roughly second-order spatial convergence when it comes to equal densities across the interface, with **M1** and **M2** displaying nearly identical behavior, whereas **M3** does marginally better with lower errors for all resolutions. When it comes to $\rho_l/\rho_g = 10$ in figure 5.18, we observe a saturation in the initial second-order convergence rate irrespective of whichever method is used, however **M3** performs slightly better in terms of error when compared **M1** and **M2**. Finally, figure 5.19 demonstrates the roughly second-order convergence of all three methods when it comes to the air-water configuration, again, with **M3** performing merginally better with lower errors. Not surprisingly, the largest errors arise for the air-water configuration errors across all methods.

Physics of Fragmentation

Ligament Mediated Paradigm 6

6.1 Mechanism of Drop Formation

Disintegration of Jets & Shear Layers Hello, here is some text without a meaning. This text should show what a printed text will look like at this place. If you read this text, you will get no information. Really? Is there no information? Is there a difference between this text and some nonsense like "Huardest gefburn"? Kjift – not at all! A blind text like this gives you information about the selected font, how the letters are written and an impression of the look. This text should contain all letters of the alphabet and it should be written in of the original language. There is no need for special content, but the length of words should match the language.

Expansion of Sheets Hello, here is some text without a meaning. This text should show what a printed text will look like at this place. If you read this text, you will get no information. Really? Is there no information? Is there a difference between this text and some nonsense like "Huardest gefburn"? Kjift – not at all! A blind text like this gives you information about the selected font, how the letters are written and an impression of the look. This text should contain all letters of the alphabet and it should be written in of the original language. There is no need for special content, but the length of words should match the language.

Effervescent Atomization Hello, here is some text without a meaning. This text should show what a printed text will look like at this place. If you read this text, you will get no information. Really? Is there no information? Is there a difference between this text and some nonsense like "Huardest gefburn"? Kjift – not at all! A blind text like this gives you information about the selected font, how the letters are written and an impression of the look. This text should contain all letters of the alphabet and it should be written in of the original language. There is no need for special content, but the length of words should match the language.

Drop Impacts Hello, here is some text without a meaning. This text should show what a printed text will look like at this place. If you read this text, you will get no information. Really? Is there no information? Is there a difference between this text and some nonsense like "Huardest gefburn"? Kjift – not at all! A blind text like this gives you information about the selected font, how the letters are written and an impression of the look. This text should contain all letters of the alphabet and it should be written in of the original language. There is no need for special content, but the length of words should match the language.

6.2 Theories of Fragmentation

Cascade Mechanism : Log-Normal Distribution Hello, here is some text without a meaning. This text should show what a printed text will look like at this place. If you read this text, you will get no information. Really? Is there no information? Is there a difference between this text and some nonsense like "Huardest gefburn"? Kjift – not at all! A blind text like this gives you information about the selected font, how the letters are written and an impression of the look. This text should contain all letters of the alphabet and it should be written in of the original language. There is no need for special content, but the length of words should match the language.

Corrugation-Coalescence Mechanism : Gamma Distribution Hello, here is some text without a meaning. This text should show what a printed text will look like at this place. If you read this text, you will get no information. Really? Is there no information? Is there a difference between this text and some nonsense like "Huardest gefburn"? Kjift – not at all! A blind text like this gives you information about the selected font, how the letters are written and an impression of the look. This text should contain all letters of the alphabet and it should be written in of the original language. There is no need for special content, but the length of words should match the language.

7 Droplet Generation in Corrugated Ligaments

7.1 Numerical Setup

Platform : Basilisk Hello, here is some text without a meaning. This text should show what a printed text will look like at this place. If you read this text, you will get no information. Really? Is there no information? Is there a difference between this text and some nonsense like "Huardest gefburn"? Kjift – not at all! A blind text like this gives you information about the selected font, how the letters are written and an impression of the look. This text should contain all letters of the alphabet and it should be written in of the original language. There is no need for special content, but the length of words should match the language.

Computational Schematic Hello, here is some text without a meaning. This text should show what a printed text will look like at this place. If you read this text, you will get no information. Really? Is there no information? Is there a difference between this text and some nonsense like "Huardest gefburn"? Kjift – not at all! A blind text like this gives you information about the selected font, how the letters are written and an impression of the look. This text should contain all letters of the alphabet and it should be written in of the original language. There is no need for special content, but the length of words should match the language.

Random Surface Generation Hello, here is some text without a meaning. This text should show what a printed text will look like at this place. If you read this text, you will get no information. Really? Is there no information? Is there a difference between this text and some nonsense like "Huardest gefburn"? Kjift – not at all! A blind text like this gives you information about the selected font, how the letters are written and an impression of the look. This text should contain all letters of the alphabet and it should be written in of the original language. There is no need for special content, but the length of words should match the language.

Parameterization Hello, here is some text without a meaning. This text should show what a printed text will look like at this place. If you read this text, you will get no information. Really? Is there no information? Is there a difference between this text and some nonsense like "Huardest gefburn"? Kjift – not at all! A blind text like this gives you information about the selected font, how the letters are written and an impression of the look. This text should contain all letters of the alphabet and it should be written in of the original language. There is no need for special content, but the length of words should match the language.

7.2 Ligament Breakup

3D vs. 2D Simulations Hello, here is some text without a meaning. This text should show what a printed text will look like at this place. If you read this text, you will get no information. Really? Is there no information? Is there a difference between this text and some nonsense like "Huardest gefburn"? Kjift – not at all! A blind text like this gives you information about the selected font, how the letters are written and an impression of the look. This text should contain all letters of the alphabet and it should be written in of the original language. There is no need for special content, but the length of words should match the language.

Effect of Spatial Resolution Hello, here is some text without a meaning. This text should show what a printed text will look like at this place. If you read this text, you will get no information. Really? Is there no information? Is there a difference between this text and some nonsense like "Huardest gefburn"? Kjift – not at all! A blind text like this gives you information about the selected font, how the letters are written and an impression of the look. This text should contain all letters of the alphabet and it should be written in of the original language. There is no need for special content, but the length of words should match the language.

Effect of Droplet Removal Hello, here is some text without a meaning. This text should show what a printed text will look like at this place. If you read this text, you will get no information. Really? Is there no information? Is there a difference between this text and some nonsense like "Huardest gefburn"? Kjift – not at all! A blind text like this gives you information about the selected font, how the letters are written and an impression of the look. This text should contain all letters of the alphabet and it should be written in of the original language. There is no need for special content, but the length of words should match the language.

Effect of Corrugation Amplitude Hello, here is some text without a meaning. This text should show what a printed text will look like at this place. If you read this text, you will get no information. Really? Is there no information? Is there a difference between this text and some nonsense like "Huardest gefburn"? Kjift – not at all! A blind text like this gives you information about the selected font, how the letters are written and an impression of the look. This text should contain all letters of the alphabet and it should be written in of the original language. There is no need for special content, but the length of words should match the language.

Effect of Ohnesorge Number Hello, here is some text without a meaning. This text should show what a printed text will look like at this place. If you read this text, you will get no information. Really? Is there no information? Is there a difference between this text and some nonsense like "Huardest gefburn"? Kjift – not at all! A blind text like this gives you information about the selected font, how the letters are written and an impression of the look. This text should contain all letters of the alphabet and it should be written in of the original language. There is no need for special content, but the length of words should match the language.

Effect of Cut-Off Wavenumber Hello, here is some text without a meaning. This text should show what a printed text will look like at this place. If you read this text, you will get no information. Really? Is there no information? Is there a difference between this text and some nonsense like "Huardest gefburn"? Kjift – not at all! A blind text like this gives you information about the selected font, how the letters are written and an impression of the look. This text should contain all letters of the alphabet and it should be written in of the original language. There is no need for special content, but the length of words should match the language.

Effect of Aspect Ratio Hello, here is some text without a meaning. This text should show what a printed text will look like at this place. If you read this text, you will get no information. Really? Is there no information? Is there a difference between this text and some nonsense like "Huardest gefburn"? Kjift – not at all! A blind text like this gives you information about the selected font, how the letters are written and an impression of the look. This text should contain all letters of the alphabet and it should be written in of the original language. There is no need for special content, but the length of words should match the language.

Quantization of Waves Hello, here is some text without a meaning. This text should show what a printed text will look like at this place. If you read this text, you will get no information. Really? Is there no information? Is there a difference between this text and some nonsense like "Huardest gefburn"? Kjift – not at all! A blind text like this gives you information about the selected font, how the letters are written and an impression of the look. This text should contain all letters of the alphabet and it should be written in of the original language. There is no need for special content, but the length of words should match the language.

Statistics of Drop Sizes 8

8.1 Monte Carlo Approach to DNS

Characterization of Ligament Ensembles Hello, here is some text without a meaning. This text should show what a printed text will look like at this place. If you read this text, you will get no information. Really? Is there no information? Is there a difference between this text and some nonsense like "Huardest gefburn"? Kjift – not at all! A blind text like this gives you information about the selected font, how the letters are written and an impression of the look. This text should contain all letters of the alphabet and it should be written in of the original language. There is no need for special content, but the length of words should match the language.

8.2 Millimeter Scale Ensembles

Diameter Distributions Hello, here is some text without a meaning. This text should show what a printed text will look like at this place. If you read this text, you will get no information. Really? Is there no information? Is there a difference between this text and some nonsense like "Huardest gefburn"? Kjift – not at all! A blind text like this gives you information about the selected font, how the letters are written and an impression of the look. This text should contain all letters of the alphabet and it should be written in of the original language. There is no need for special content, but the length of words should match the language.

Mass Distributions Hello, here is some text without a meaning. This text should show what a printed text will look like at this place. If you read this text, you will get no information. Really? Is there no information? Is there a difference between this text and some nonsense like "Huardest gefburn"? Kjift – not at all! A blind text like this gives you information about the selected font, how the letters are written and an impression of the look. This text should contain all letters of the alphabet and it should be written in of the original language. There is no need for special content, but the length of words should match the language.

Equivalent Diameters Hello, here is some text without a meaning. This text should show what a printed text will look like at this place. If you read this text, you will get no information. Really? Is there no information? Is there a difference between this text and some nonsense like "Huardest gefburn"? Kjift – not at all! A blind text like this gives you information about the selected font, how the letters are written and an impression of the look. This text should contain all letters of the alphabet and it should be written in of the original language. There is no need for special content, but the length of words should match the language.

Local Distribution of Large Drop Sizes Hello, here is some text without a meaning. This text should show what a printed text will look like at this place. If you read this text, you will get no information. Really? Is there no information? Is there a difference between this text and some nonsense like "Huardest gefburn"? Kjift – not at all! A blind text like this gives you information about the selected font, how the letters are written and an impression of the look. This text should contain all letters of the alphabet and it should be written in of the original language. There is no need for special content, but the length of words should match the language.

8.3 Exploration of Parameter Space Φ

Bifurcation Parameter : Corrugation Amplitude Hello, here is some text without a meaning. This text should show what a printed text will look like at this place. If you read this text, you will get no information. Really? Is there no information? Is there a difference between this text and some nonsense like "Huardest gefburn"? Kjift – not at all! A blind text like this gives you information about the selected font, how the letters are written and an impression of the look. This text should contain all letters of the alphabet and it should be written in of the original language. There is no need for special content, but the length of words should match the language.

Scaling of D/W : Function of Parameter Space Hello, here is some text without a meaning. This text should show what a printed text will look like at this place. If you read this text, you will get no information. Really? Is there no information? Is there a difference between this text and some nonsense like "Huardest gefburn"? Kjift – not at all! A blind text like this gives you information about the selected font, how the letters are written and an impression of the look. This text should contain all letters of the alphabet and it should be written in of the original language. There is no need for special content, but the length of words should match the language.

To be added Hello, here is some text without a meaning. This text should show what a printed text will look like at this place. If you read this text, you will get no information. Really? Is there no information? Is there a difference between this text and some nonsense like "Huardest gefburn"? Kjift – not at all! A blind text like this gives you information about the selected font, how the letters are written and an impression of the look. This text should contain all letters of the alphabet and it should be written in of the original language. There is no need for special content, but the length of words should match the language.

Conclusions & Perspectives

Hello, here is some text without a meaning. This text should show what a printed text will look like at this place. If you read this text, you will get no information. Really? Is there no information? Is there a difference between this text and some nonsense like “Huardest gefburn”? Kjift – not at all! A blind text like this gives you information about the selected font, how the letters are written and an impression of the look. This text should contain all letters of the alphabet and it should be written in of the original language. There is no need for special content, but the length of words should match the language.

This is the second paragraph. Hello, here is some text without a meaning. This text should show what a printed text will look like at this place. If you read this text, you will get no information. Really? Is there no information? Is there a difference between this text and some nonsense like “Huardest gefburn”? Kjift – not at all! A blind text like this gives you information about the selected font, how the letters are written and an impression of the look. This text should contain all letters of the alphabet and it should be written in of the original language. There is no need for special content, but the length of words should match the language.

And after the second paragraph follows the third paragraph. Hello, here is some text without a meaning. This text should show what a printed text will look like at this place. If you read this text, you will get no information. Really? Is there no information? Is there a difference between this text and some nonsense like “Huardest gefburn”? Kjift – not at all! A blind text like this gives you information about the selected font, how the letters are written and an impression of the look. This text should contain all letters of the alphabet and it should be written in of the original language. There is no need for special content, but the length of words should match the language.

After this fourth paragraph, we start a new paragraph sequence. Hello, here is some text without a meaning. This text should show what a printed text will look like at this place. If you read this text, you will get no information. Really? Is there no information? Is there a difference between this text and some nonsense like “Huardest gefburn”? Kjift – not at all! A blind text like this gives you information about the selected font, how the letters are written and an impression of the look. This text should contain all letters of the alphabet and it should be written in of the original language. There is no need for special content, but the length of words should match the language.

Hello, here is some text without a meaning. This text should show what a printed text will look like at this place. If you read this text, you will get no information. Really? Is there no information? Is there a difference between this text and some nonsense like “Huardest gefburn”? Kjift – not at all! A blind text like this gives you information about the selected font, how the letters are written and an impression of the look. This text should contain all letters of the alphabet and it should be written in of the original language. There is no need for special content, but the length of words should match the language.

Appendix

A

Heading on Level 0 (chapter)

Hello, here is some text without a meaning. This text should show what a printed text will look like at this place. If you read this text, you will get no information. Really? Is there no information? Is there a difference between this text and some nonsense like “Huardest gefburn”? Kjift – not at all! A blind text like this gives you information about the selected font, how the letters are written and an impression of the look. This text should contain all letters of the alphabet and it should be written in of the original language. There is no need for special content, but the length of words should match the language.

A.1 Heading on Level 1 (section)

Hello, here is some text without a meaning. This text should show what a printed text will look like at this place. If you read this text, you will get no information. Really? Is there no information? Is there a difference between this text and some nonsense like “Huardest gefburn”? Kjift – not at all! A blind text like this gives you information about the selected font, how the letters are written and an impression of the look. This text should contain all letters of the alphabet and it should be written in of the original language. There is no need for special content, but the length of words should match the language.

Heading on Level 2 (subsection)

Hello, here is some text without a meaning. This text should show what a printed text will look like at this place. If you read this text, you will get no information. Really? Is there no information? Is there a difference between this text and some nonsense like “Huardest gefburn”? Kjift – not at all! A blind text like this gives you information about the selected font, how the letters are written and an impression of the look. This text should contain all letters of the alphabet and it should be written in of the original language. There is no need for special content, but the length of words should match the language.

Heading on Level 3 (subsubsection)

Hello, here is some text without a meaning. This text should show what a printed text will look like at this place. If you read this text, you will get no information. Really? Is there no information? Is there a difference between this text and some nonsense like “Huardest gefburn”? Kjift –

not at all! A blind text like this gives you information about the selected font, how the letters are written and an impression of the look. This text should contain all letters of the alphabet and it should be written in of the original language. There is no need for special content, but the length of words should match the language.

Heading on Level 4 (paragraph) Hello, here is some text without a meaning. This text should show what a printed text will look like at this place. If you read this text, you will get no information. Really? Is there no information? Is there a difference between this text and some nonsense like "Huardest gefburn"? Kjift – not at all! A blind text like this gives you information about the selected font, how the letters are written and an impression of the look. This text should contain all letters of the alphabet and it should be written in of the original language. There is no need for special content, but the length of words should match the language.

A.2 Lists

Example for list (itemize)

- First item in a list
- Second item in a list
- Third item in a list
- Fourth item in a list
- Fifth item in a list

Example for list (4*itemize)

- First item in a list
  - First item in a list
    - First item in a list
      - First item in a list
      - Second item in a list
    - Second item in a list
  - Second item in a list
- Second item in a list

Example for list (enumerate)

1. First item in a list
2. Second item in a list
3. Third item in a list
4. Fourth item in a list
5. Fifth item in a list

Example for list (4*enumerate)

1. First item in a list
    a) First item in a list
        i. First item in a list
            A. First item in a list
            B. Second item in a list
        ii. Second item in a list
    b) Second item in a list
2. Second item in a list

Example for list (description)

First item in a list
Second item in a list
Third item in a list
Fourth item in a list
Fifth item in a list

Example for list (4*description)

First item in a list
    First item in a list
        First item in a list
            First item in a list
            Second item in a list
        Second item in a list
    Second item in a list
Second item in a list

Bibliography

Here are the references in citation order.

[1] W Aniszewski et al. 'PArallel, Robust, Interface Simulator (PARIS)'. In: (2019) (cited on pages 4, 7, 12, 14, 24).

[2] S Popinet. 'Basilisk, a Free-Software program for the solution of partial differential equations on adaptive Cartesian meshes (2018)'. In: *URL http://basilisk. fr* () (cited on pages 4, 7, 12).

[3] Cyril W Hirt and Billy D Nichols. 'Volume of fluid (VOF) method for the dynamics of free boundaries'. In: *Journal of computational physics* 39.1 (1981), pp. 201–225 (cited on page 6).

[4] Stanley Osher and James A Sethian. 'Fronts propagating with curvature-dependent speed: algorithms based on Hamilton-Jacobi formulations'. In: *Journal of computational physics* 79.1 (1988), pp. 12–49 (cited on page 6).

[5] Grétar Tryggvason, Ruben Scardovelli, and Stéphane Zaleski. *Direct numerical simulations of gas–liquid multiphase flows*. Cambridge University Press, 2011 (cited on pages 6, 8).

[6] Stéphane Popinet. 'Numerical models of surface tension'. In: *Annual Review of Fluid Mechanics* 50 (2018), pp. 49–75 (cited on pages 6, 24, 45).

[7] Ruben Scardovelli and Stéphane Zaleski. 'Direct numerical simulation of free-surface and interfacial flow'. In: *Annual review of fluid mechanics* 31.1 (1999), pp. 567–603 (cited on pages 6–8).

[8] Ruben Scardovelli and Stephane Zaleski. 'Interface reconstruction with least-square fit and split Eulerian–Lagrangian advection'. In: *International Journal for Numerical Methods in Fluids* 41.3 (2003), pp. 251–274 (cited on page 6).

[9] Eugenio Aulisa et al. 'Interface reconstruction with least-squares fit and split advection in three-dimensional Cartesian geometry'. In: *Journal of Computational Physics* 225.2 (2007), pp. 2301–2319 (cited on page 6).

[10] Gabriel D Weymouth and Dick K-P Yue. 'Conservative volume-of-fluid method for free-surface simulations on cartesian-grids'. In: *Journal of Computational Physics* 229.8 (2010), pp. 2853–2865 (cited on pages 7, 9, 10, 27).

[11] Shahab Mirjalili, Suhas S Jain, and Micheal Dodd. 'Interface-capturing methods for two-phase flows: An overview and recent developments'. In: *Center for Turbulence Research Annual Research Briefs* 2017 (2017), pp. 117–135 (cited on pages 7, 26).

[12] Eugenio Aulisa et al. 'A geometrical area-preserving volume-of-fluid advection method'. In: *Journal of Computational Physics* 192.1 (2003), pp. 355–364 (cited on page 8).

[13] Jie Li. 'Calcul d'interface affine par morceaux'. In: *Comptes rendus de l'Académie des sciences. Série II, Mécanique, physique, chimie, astronomie* 320.8 (1995), pp. 391–396 (cited on page 8).

[14] Denis Gueyffier et al. 'Volume-of-fluid interface tracking with smoothed surface stress methods for three-dimensional flows'. In: *Journal of Computational physics* 152.2 (1999), pp. 423–456 (cited on pages 8, 9).

[15] Randall J LeVeque. 'High-resolution conservative algorithms for advection in incompressible flow'. In: *SIAM Journal on Numerical Analysis* 33.2 (1996), pp. 627–665 (cited on pages 11, 20).

[16] Peter K Sweby. 'High resolution schemes using flux limiters for hyperbolic conservation laws'. In: *SIAM journal on numerical analysis* 21.5 (1984), pp. 995–1011 (cited on pages 11, 20).

[17] Alexandre Joel Chorin. 'On the convergence of discrete approximations to the Navier-Stokes equations'. In: *Mathematics of computation* 23.106 (1969), pp. 341–353 (cited on page 11).

[18] William L Briggs. 'A Multigrid Tutorial, SIAM'. In: *Carver, MB (1984)"Numerical Computation of Phase Separation in Two Fluid Flow," ASME Journal of Fluids Engineering* 106 (1987), pp. 147–153 (cited on page 12).

[19] Stéphane Popinet. 'Gerris: a tree-based adaptive solver for the incompressible Euler equations in complex geometries'. In: *Journal of Computational Physics* 190.2 (2003), pp. 572–600 (cited on page 12).

[20] Stéphane Popinet. 'An accurate adaptive solver for surface-tension-driven interfacial flows'. In: *Journal of Computational Physics* 228.16 (2009), pp. 5838–5866 (cited on pages 12, 13, 24, 35, 36, 39–41, 43, 45–47, 49).

[21] G Bornia et al. 'On the properties and limitations of the height function method in two-dimensional Cartesian geometry'. In: *Journal of Computational Physics* 230.4 (2011), pp. 851–862 (cited on page 13).

[22] Mark Owkes and Olivier Desjardins. 'A mesh-decoupled height function method for computing interface curvature'. In: *Journal of Computational Physics* 281 (2015), pp. 285–300 (cited on page 13).

[23] D Fuster et al. 'A momentum-conserving, consistent, Volume-of-Fluid method for incompressible flow on staggered grids'. In: *arXiv preprint arXiv:1811.12327* (2018) (cited on pages 14, 24, 27).

[24] Ross Gunn and Gilbert D Kinzer. 'The terminal velocity of fall for water droplets in stagnant air'. In: *Journal of Meteorology* 6.4 (1949), pp. 243–248 (cited on page 14).

[25] Michael S Dodd and Antonino Ferrante. 'A fast pressure-correction method for incompressible two-fluid flows'. In: *Journal of Computational Physics* 273 (2014), pp. 416–434 (cited on pages 15, 19).

[26] Feng Xiao. 'Large eddy simulation of liquid jet primary breakup'. PhD thesis. © F. Xiao, 2012 (cited on page 16).

[27] Murray Rudman. 'A volume-tracking method for incompressible multifluid flows with large density variations'. In: *International Journal for numerical methods in fluids* 28.2 (1998), pp. 357–378 (cited on pages 25, 26).

[28] Markus Bussmann, Douglas B Kothe, and James M Sicilian. 'Modeling high density ratio incompressible interfacial flows'. In: *ASME 2002 Joint US-European Fluids Engineering Division Conference*. American Society of Mechanical Engineers. 2002, pp. 707–713 (cited on page 25).

[29] Mehdi Raessi and Heinz Pitsch. 'Consistent mass and momentum transport for simulating incompressible interfacial flows with large density ratios using the level set method'. In: *Computers & Fluids* 63 (2012), pp. 70–81 (cited on page 25).

[30] S Ghods and Marcus Herrmann. 'A consistent rescaled momentum transport method for simulating large density ratio incompressible multiphase flows using level set methods'. In: *Physica Scripta* 2013.T155 (2013), p. 014050 (cited on page 25).

[31] Vincent Le Chenadec and Heinz Pitsch. 'A monotonicity preserving conservative sharp interface flow solver for high density ratio two-phase flows'. In: *Journal of Computational Physics* 249 (2013), pp. 185–203 (cited on page 25).

[32] Mark Owkes and Olivier Desjardins. 'A mass and momentum conserving unsplit semi-Lagrangian framework for simulating multiphase flows'. In: *Journal of Computational Physics* 332 (2017), pp. 21–46 (cited on page 25).

[33] G Vaudor et al. 'A consistent mass and momentum flux computation method for two phase flows. Application to atomization process'. In: *Computers & Fluids* 152 (2017), pp. 204–216 (cited on pages 25, 26).

[34] Davide Zuzio et al. 'A new efficient momentum preserving Level-Set/VOF method for high density and momentum ratio incompressible two-phase flows'. In: *Journal of Computational Physics* 410 (2020), p. 109342 (cited on pages 25, 26).

[35] Jitendra Kumar Patel and Ganesh Natarajan. 'A novel consistent and well-balanced algorithm for simulations of multiphase flows on unstructured grids'. In: *Journal of computational physics* 350 (2017), pp. 207–236 (cited on page 26).

[36] Nishant Nangia et al. 'A robust incompressible Navier-Stokes solver for high density ratio multiphase flows'. In: *Journal of Computational Physics* 390 (2019), pp. 548–594 (cited on page 26).

[37] Bruno Lafaurie et al. 'Modelling merging and fragmentation in multiphase flows with SURFER'. In: *Journal of Computational Physics* 113.1 (1994), pp. 134–147 (cited on page 35).

[38] Dalton JE Harvie, MR Davidson, and Murray Rudman. 'An analysis of parasitic current generation in volume of fluid simulations'. In: *Applied mathematical modelling* 30.10 (2006), pp. 1056–1066 (cited on page 35).

[39] Stéphane Popinet and Stéphane Zaleski. 'A front-tracking algorithm for accurate representation of surface tension'. In: *International Journal for Numerical Methods in Fluids* 30.6 (1999), pp. 775–793 (cited on pages 35, 46).

[40] Marianne M Francois et al. 'A balanced-force algorithm for continuous and sharp interfacial surface tension models within a volume tracking framework'. In: *Journal of Computational Physics* 213.1 (2006), pp. 141–173 (cited on page 35).

[41] Thomas Abadie, Joelle Aubin, and Dominique Legendre. 'On the combined effects of surface tension force calculation and interface advection on spurious currents within Volume of Fluid and Level Set frameworks'. In: *Journal of Computational Physics* 297 (2015), pp. 611–636 (cited on page 40).

[42] Horace Lamb. *Hydrodynamics*. Cambridge university press, 1993 (cited on pages 46, 47).

[43] Andrea Prosperetti. 'Free oscillations of drops and bubbles: the initial-value problem'. In: *Journal of Fluid Mechanics* 100.2 (1980), pp. 333–347 (cited on pages 46, 47).

[44] Andrea Prosperetti. 'Motion of two superposed viscous fluids'. In: *The Physics of Fluids* 24.7 (1981), pp. 1217–1223 (cited on pages 46, 47).

Notation

The next list describes several symbols that will be later used within the body of the document.

c Speed of light in a vacuum inertial frame

h Planck constant

Greek Letters with Pronounciation

Character	Name	Character	Name
α	alpha *AL-fuh*	ν	nu *NEW*
β	beta *BAY-tuh*	ξ, Ξ	xi *KSIGH*
γ, Γ	gamma *GAM-muh*	o	omicron *OM-uh-CRON*
δ, Δ	delta *DEL-tuh*	π, Π	pi *PIE*
ϵ	epsilon *EP-suh-lon*	ρ	rho *ROW*
ζ	zeta *ZAY-tuh*	σ, Σ	sigma *SIG-muh*
η	eta *AY-tuh*	τ	tau *TOW (as in cow)*
θ, Θ	theta *THAY-tuh*	υ, Υ	upsilon *OOP-suh-LON*
ι	iota *eye-OH-tuh*	ϕ, Φ	phi *FEE, or FI (as in hi)*
κ	kappa *KAP-uh*	χ	chi *KI (as in hi)*
λ, Λ	lambda *LAM-duh*	ψ, Ψ	psi *SIGH, or PSIGH*
μ	mu *MEW*	ω, Ω	omega *oh-MAY-guh*

Capitals shown are the ones that differ from Roman capitals.